2009

Design and Development of a Ka-band Interferometer for Cryospheric Applications

Harish K. Vedantham
University of Massachusetts Amherst

DESIGN AND DEVELOPMENT OF A KA-BAND INTERFEROMETER FOR CRYOSPHERIC APPLICATIONS

A Thesis Presented

by

HARISH VEDANTHAM

Submitted to the Graduate School of the
University of Massachusetts Amherst in partial fulfillment
of the requirements for the degree of

MASTER OF SCIENCE IN ELECTRICAL AND COMPUTER ENGINEERING

February 2009

Electrical and Computer Engineering

DESIGN AND DEVELOPMENT OF A KA-BAND INTERFEROMETER FOR CRYOSPHERIC APPLICATIONS

A Thesis Presented

by

HARISH VEDANTHAM

Approved as to style and content by:

Paul R. Siqueira, Chair

Stephen J. Frasier, Member

Daniel H. Schaubert, Member

Christopher V. Hollot, Department Chair
Electrical and Computer Engineering

For my mother, father and sister

This Earth is His, to Him belong
those vast and boundless skies,
Both seas within Him rest, and yet
in that small pool He lies.

Atharva Veda
12^{th} century BC

ACKNOWLEDGMENTS

I have had an enjoyable and rewarding time working at the Microwave Remote Sensing Lab. The process of learning, better yet, the process of learning to learn and to appreciate things- small and big, simple and intricate have left a gratifying feeling in me. For giving me an oppurtunity to go through this learning process in both my personal and professional life, I feel indebted to Dr. Paul Siqueira; perhaps more so for his guidance, patience and confidence in my abilities. I am also thankful to Dr. Stephen Frasier and Dr. Daniel Schaubert for reviewing my research work, and providing me with feedback while serving on my thesis committee.

While the professors taught me the "elegant theory", Edin Insanić, my friend and colleague mentored me through the hands-on aspect of research- of being "street-smart" and "dirtying my hands in the lab" which were his phrases to denote that bundle of applied practical knowledge he gave me, which I could never find in books, and without which I could not have built a radar from scratch. Words are perhaps not enough to express my gratitude to Edin for his patience and selfless help.

I feel thankful to my friends at MIRSL who have been of constant support and a source of fun and frolic that has kept me cheerful despite the rigours of graduate life. To Razi for being *Razi bhai*, to Pei for her patient help, to Tao, Matt and Joe for their jestful company, to Vijay for his frankness and selfless help, and to Iva for the care and warmth of her presence.

Above everything else, I feel thankful to my mother and father for their unconditional love and support, and to my sister for the sheer joy she brings to my everyday life.

TABLE OF CONTENTS

LIST OF TABLES

Table **Page**

LIST OF FIGURES

Figure **Page**

CHAPTER 1

INTRODUCTION

1.1 History and Motivation

Topographic maps of the earth are essential to geographic and earth science studies. In particular, mapping and estimating physical parameters of the earth's water and ice cover are critical to global climate studies. Among these, snow, ocean and fresh water topography, snow wetness and water equivalent are of immediate interest to the scientific community. Snow topography measurement finds use in global snow content estimation for earth's energy balance and global warming studies. Ocean topography studies help in ocean energy content estimation for predicting climatic phenomena such as the El Niño. Apart from topography, snow wetness and snow water equivalent are important variables in the prediction of freshwater availability due to snow-melt in summer.

Challenges in the instrument development and deployment posed by these required measurements are twofold. Firstly, these measurements are required to have global coverage, yet maintain stringent spatial resolution and accuracy margins. Secondly, snow topography measurement requires minimal electromagnetic wave penetration through snow, hence requiring the use of millimeter-wave frequency radars. While having the advantage of smaller and lighter structures, instruments at millimeter-wave frequencies are difficult to design, evaluate and deploy due to their mechanical and electric precision requirements.

Despite such challenges, several airborne and spaceborne missions to measure ocean and snow topography have been successfully flown. NASA's Ocean Surface and

Topography Mission[†] (OSTM-1 and OSTM-2) have retrieved global ocean topography through dual-frequency altimetry. Altimetric measurements have good height accuracy but are point measurements and lack the mapping ability of a side-looking radar. On the other hand, single-pass interferometric synthetic aperture radar missions such as SRTM[‡] (Shuttle Radar Topography Mission), GeoSAR and UAVSAR[§] have demonstrated mapping capability with good height accuracy but such campaigns are limited to X-band and lower frequencies where high snow penetration is a problem in cryospheric mapping. While campaign quality millimeter-wave spaceborne instruments exist, (see NASA's PR-2 for instance) interferometric mapping capability from an airborne or spaceborne platform at millimeter-wave frequencies is yet to be demonstrated. To address this current need of the scientific community, the National Research Council identified Ku- and Ka-band interferometers as key technologies for oceanic and cryospheric mapping in the upcoming decade.

Accurate interferometric mapping at Ka-band requires a new regime of phase-stability between the two channels of the interferometer receiver over different operating conditions despite undergoing non-linear downconversion operations in hardware. Algorithms for precise estimation of the two-channel phase are required for phase stability characterization and phase calibration of the instrument. This makes the design and evaluation of the downconverter a formidable challenge in Ka-band interferometry. Through a project funded by a NASA grant awarded to the University of Massachusetts under the Advanced Component Technology (ACT) program, an effort has been ongoing to refine the design, development and testing of a Ka-band two-channel downconverter for these purposes. Additionally, a transmitter, antennas, signal generation and data acquisition units are being designed to support the appli-

[†]See http://topex-www.jpl.nasa.gov/mission/ostm.html

[‡]See http://www2.jpl.nasa.gov/srtm/

[§]See http://uavsar.jpl.nasa.gov/

cation of this downconverter in the field as part of a working interferometric radar. Topographic measurements made with this instrument deployed on a static platform such as a rooftop will result in characterization of instrument errors and identification of dominant error sources. The design, development and deployment of the Ka-band interferometer will not only serve as a proof of concept, but also as a benchmark for future airborne and spaceborne missions.

1.2 Summary of chapters

Chapter 2 presents the basic theory of radar interferometry and cross-track interferometric mapping. Important issues influencing the choice of interferometric parameters such as sensitivity, ambiguity and error are discussed. Chapter 3 applies these concepts to arrive at a choice of instrument architecture and radar parameters in terms of hardware and deployment geometry. Chapter 4 describes the detailed design and development of the transmitter, receiver, signal generation, data acquisition, control circuitry and antennas making up the radar hardware. Chapter 5 presents the results from laboratory evaluation of the radar hardware in terms of bandpass characterization and thermal stability evaluation of the receiver, and antenna pattern measurement. A detailed description of the experimental setup and phase estimation algorithm used for bandpass phase stability characterization of the downconverter is documented. Results from the thermal characterization of the downconverter bandpass characteristics are presented. Chapter 6 describes the experimental setup of the first deployment of the downconverter as part of an interferometer on ground and on the rooftop of the LGRT (Lederle Graduate Research Center) at the University of Massachusetts, Amherst. First results and lessons learnt from these deployments are documented. Chapter 7 summarizes the research carried out, and presents the conclusions and recommendations to aid future work.

CHAPTER 2

INTERFEROMETRY AND TOPOGRAPHIC MAPPING

Radar interferometers in different configurations have been used for mapping topography and topographic change. This chapter discusses the fundamental principle of radar interferometry. Different interferometric configurations are discussed briefly, and the theory of topographic mapping with cross-track interferometry is presented. Issues affecting the choice of interferometric parameters in the design space are discussed for a generic cross-track interferometer.

2.1 Radar Interferometry

Interferometry is a technique of superimposing two coherent electric fields separated spatially and/or temporally. The constructive and destructive interference of the electric fields in the spatial and/or temporal domain forms interference patterns which carry the information of interest. Although interferometry has been extensively used by optical and plasma physicists for more than two centuries, the remote sensing community has been using radar interferometers only recently. The earliest documented use of radar interferometry was for extra-terrestrial mapping of Venus [14] and the moon [19]. Graham was the first to demonstrate its use for terrestrial mapping using synthetic aperture radars [3]. Graham recorded the beat or interference pattern of two spatially separated radar receive channels on a moving film. More recently, after the advent of computer processing and storage, Zebker and Goldstein [18] demonstrated airborne interferometry by digitizing and recording the signal from two spatially separated RF receivers to form the interference patterns in post process-

ing. Soon spaceborne interferometry was demonstrated by Goldstein et al [2] using data from SEASAT. Currently, tens of airborne and spaceborne interferometers are in commission which provide commercial interferometric data and data products. A discussion of the basic theory of operation used by all of the above interferometers follows.

Radar interferometers sample the electric field scattered by a target using radar receivers separated spatially and/or temporally. Samples of the two received electric fields are interfered to compute the phase difference between them. Using a simple geometric transformation, this phase difference is used to accurately estimate topography and topographic change. Depending on their application, radar interferometers can have different configurations. Single-pass interferometers simultaneously acquire radar returns on two (or more) receive channels which are separated by a spatial vector called baseline. Repeat-pass interferometers acquire temporally (and possibly spatially) separated radar returns on a single channel forming a temporal (and possibly spatial) vector baseline. If the spatial baseline is oriented perpendicular to the flight track of the aircraft or spacecraft then the interferometer is called a cross-track interferometer. This type of interferometer is sensitive to topographic height variations. If the baseline is oriented parallel to the flight track, the interferometer is called an along-track interferometer. This type of interferometer is sensitive to the target's radial velocity. Figure 2.1 depicts these naming conventions.

The two channels of a single-pass interferometer can be configured in two modes of operation. When both channels transmit alternate radar pulses, the mode is termed ping-pong mode. When only one of the channels transmit, the mode is termed non-ping-pong mode or normal mode. The effective baseline in ping-pong mode can be shown to be twice the physical baseline. This gives the ping-pong mode advantage in low frequency (L-band and lower) interferometry requiring large baselines despite its drawback of increased circuit complexity.

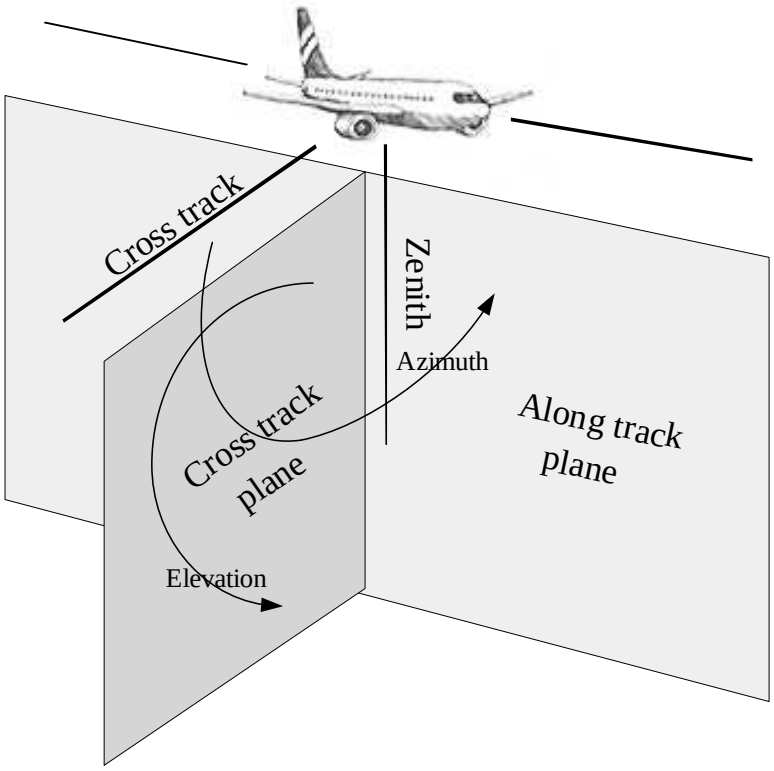

Figure 2.1. Naming conventions for a single-pass interferometer

These different instrument configurations can be used to derive different functionalities. Cross-track single pass and repeat-pass interferometers can be used to estimate topography. Single pass along-track interferometers have small temporal baselines, and can be used to estimate the speed of water currents and mobile terrestrial targets. The temporal baseline of the repeat pass interferometers is on larger time scales, and can be used to estimate topographic change. The main subject of this thesis is a single pass cross-track interferometer operating in the normal mode. Analytical formulation of such a mapping geometry follows.

2.2 Topographic height mapping

Conventional airborne radars can measure the along-track and cross-track location of the target through measurement of range and doppler. Assuming a stationary

target, doppler shift results from the aircraft's motion and bearing relative to the target. Iso-range targets lie on the surface of a sphere concentric with the radar, and iso-doppler scatterers lie on the surface of a cone co-axial with the flight track. The intersection of an iso-range sphere and an iso-doppler cone is a circular locus. The antenna beam may reduce the ambiguity in target location within this locus, but to a very limited extent. To obtain a three-dimensional target position, another (preferably independent) measurement is required. Cross-track interferometry provides this measurement in the form of look angle to target. This look angle is computed using the phase difference between the two receive channels.

Figure 2.2 depicts the geometry of a cross-track interferometer where the along-track vector goes into the plane of the paper. The interferometer achieves coverage in the cross-track direction with a wide antenna beam and in the along-track direction through flight, or in the case of a static deployment, through azimuth steering. Resolution in the cross-track direction is achieved through radar ranging. Resolution in the along-track plane is achieved through aperture synthesis or a narrow antenna azimuth beamwidth. The phase difference between A1 and A2 of the wave scattered from each of these resolution elements can be related to their height through geometric transformations using (2.1).

$$\Delta r = \frac{\Delta\phi\lambda}{2\pi} \tag{2.1a}$$

$$\nu = \cos^{-1}\left(\frac{B^2 + r^2 - (r+\Delta r)^2}{2Br}\right) \tag{2.1b}$$

$$h = H - r\cos(\gamma + \nu) \tag{2.1c}$$

It can be seen that knowledge of the vector baseline (B and γ) and path length difference (Δr) gives the look angle that can be used to estimate height. Assuming minimal volumetric scattering, and by tessellating the heights of various resolution

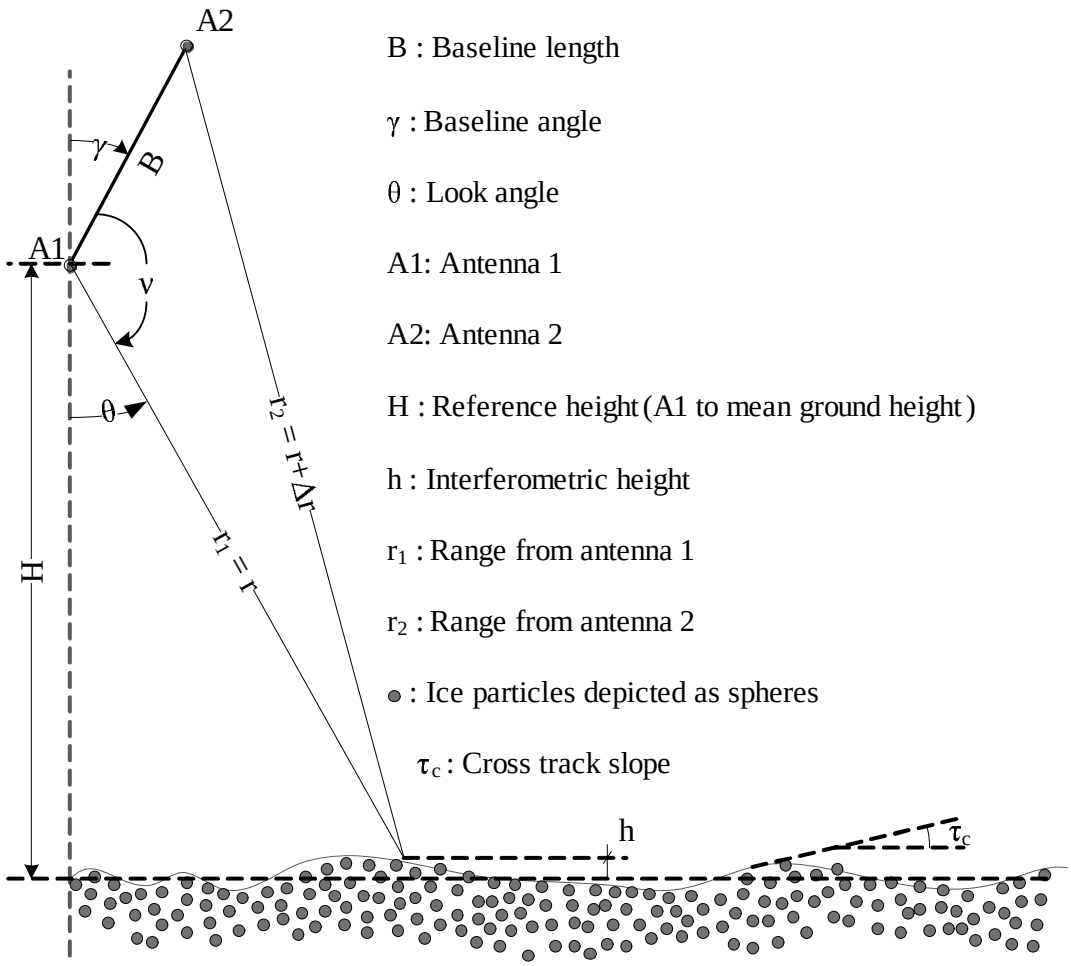

Figure 2.2. Geometry of a cross-track interferometer

cells, an elevation profile can be constructed. This is the basic principle of cross-track interferometric mapping.

In practice, owing to the finite spatial resolutions in the cross-track (or elevation) and along-track (or azimuth) planes, the electric field received by either antennas is a vector sum of the contributions from all scatterers from within a resolution element. The locations and scattering properties of these scatterers is not deterministic in case of natural media, and the measured backscattered electric fields are random variables. These electric fields received at the two antennas are represented by their ensemble average over scatterer locations and scattering properties as $\langle \mathbf{E_1} \rangle$ and $\langle \mathbf{E_2} \rangle$. The cross-

correlation between them given by $\langle \mathbf{E_1} \rangle \langle \mathbf{E_2^*} \rangle = \langle \mathbf{E_1 E_2^*} \rangle^{\dagger}$ is called the interferogram. The argument of the interferogram in the complex phasor domain is the inter-channel phase difference $\Delta\phi$, used in (2.1). The cross-correlation coefficient between the two received fields is indicative of the extent of coherence between the two receive channels and is given by

$$\rho = \frac{\langle \mathbf{E_1 E_2^*} \rangle}{\sqrt{\langle \mid \mathbf{E_1} \mid^{\mathbf{2}} \rangle \langle \mid \mathbf{E_2} \mid^{\mathbf{2}} \rangle}}. \tag{2.2}$$

To understand the effect of the spatial extent of a resolution element on the coherence, and the effect of this coherence on the performance of the interferometer, a discussion on the resolution, sensitivity, and accuracy of the instrument is imperative.

2.3 Resolution and sensitivity

Knowledge of resolution, sensitivity, and ambiguity of the instrument is of prime importance. As mentioned earlier, cross-track resolution is related to the radar bandwidth, and in simple terms is the projection of the range resolution on the cross-track plane. It is given by,

$$\delta r_{el} \approx \frac{c}{2\Delta f}. \sin(\theta - \tau_c). \tag{2.3}$$

Here, c is the speed of light in free space, Δf is the radar bandwidth, $\frac{c}{2\Delta f}$ is the range resolution of the radar, and $\sin(\theta - \tau_c)$ is the projection factor. Along-track resolution in case of aperture synthesis can be as low as half the physical length of the antenna. In case of a real aperture radar, it is related to the antenna azimuth beamwidth, Φ_{bw}, as

$$\delta r_{az} \approx r\Phi_{bw} = \frac{H\Phi_{bw}}{\cos(\theta)}. \tag{2.4}$$

[†]This equality holds only in sparse random media where the probability densities of scatterer position and scattering characteristics are independent of one another. This assumption is made here for simplicity.

Cross-track and along-track ground resolutions are different from resolution in the measurement of phase, the estimation of which is a much more involved task. The theory behind phase estimation will be dealt with in Chapter 5.

Sensitivity is a measure of the rate of change of phase with ground height. Due to the side-looking nature of the radar, sensitivity to elevation slope is far greater than sensitivity to azimuth slope. Sensitivity to elevation slope has a paramount influence on the design parameters and unless mentioned otherwise, sensitivity in this document implies sensitivity in elevation.

Phase sensitivity to height increases with increasing baseline, frequency, and as the cross-track slope becomes parallel to the baseline. The rate of change of phase (disregrading the curvature of the earth) is given by [10]

$$\frac{\partial(\Delta\phi)}{\partial r} = \frac{\partial(\Delta\phi)}{\partial\theta}\,\frac{\partial\theta}{\partial r} = \frac{2\pi}{\lambda}\,B\sin(\theta+\gamma)\,\frac{1}{r\sin(\theta)}\,\left[\cos(\theta)+\frac{\sin(\tau_c)}{\sin(\theta-\tau_c)}\right] \qquad (2.5)$$

where τ_c is the cross-track slope (see Figure 2.2). As discussed earlier, returns from within a resolution element are indistinguishable, and the observed return is a vector sum of the fields scattered from within a resolution element. This effect of finite resolution and sensitivity is depicted in Figure 2.3. Scatterers within a resolution cell (depicted as circles), their vector contribution to the interferogram (grey vectors), and the resultant interferogram are shown. If the rate of change of phase in (2.5) approaches 2π radians within one resolution element, the returns from induvidual elements will not add to a well defined phase. Not only that, a high rate of change of phase creates problems in unwrapping the phase ambiguity. In statistical terms, as the change in interferometric phase within a resolution element increases, the fields received at the two channels loose coherence, thereby lowering their correlation coefficient (see (2.2)) and hence, this effect is also termed geometric decorrelation. Geometric decorrelation is also referred to as baseline decorrelation since phase sensitivity is tightly related to baseline length and angle.

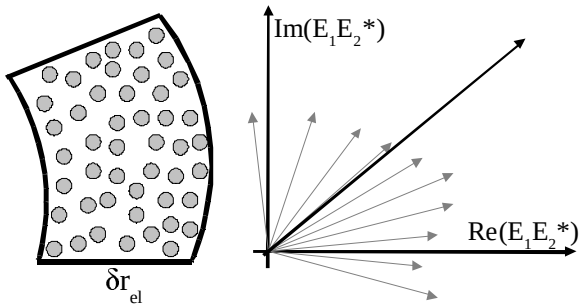

Figure 2.3. Depiction of the spatial extent of a resolution element giving geometric decorrelation

Another effect of sensitivity and modulo 2π nature of phase is height ambiguity. Height ambiguity is the change in topographic height that would result in a 2π phase wrap, and thus would be indistinguishable. Height ambiguity, h_a is given by [10]

$$h_a = 2\pi . \frac{\partial h}{\partial(\Delta\phi)} = \frac{\lambda r \sin(\theta)}{B\cos(\theta + \gamma)}. \tag{2.6}$$

As in any instrument, sensitivity and accuracy are conflicting parameters, and it is a trade-off between them that has to be understood to arrive at a good design. An account of height accuracy follows.

2.4 Accuracy

The error analysis used here is the one presented by Faller and Meier [8]. Figure 2.4 shows the interdependency of variables in an interferometric height extraction. It

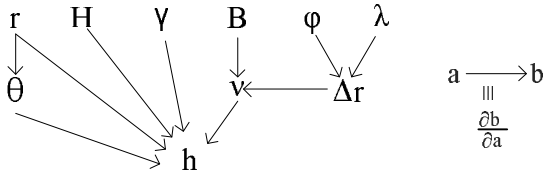

Figure 2.4. Relationship between variables and propagation of errors in an interferometric height extraction

depicts the manner in which measurement errors propagate to contribute to the final

height error. Variables at the top are the primary measurables. Link from variable a to variable b represents the sensitivity in b to change in a, $\frac{\partial b}{\partial a}$. These link arrows acting like scaling factors to the errors in the primary measurables. The resultant height error is given by,

$$e_h^2 = A_r^2 e_r^2 + A_B^2 e_B^2 + A_H^2 e_H^2 + A_\gamma^2 e_\gamma^2 + A_\phi^2 e_\phi^2 + A_\lambda^2 e_\lambda^2. \tag{2.7}$$

Here, e_H is the RMS error in deployment height, e_B is the RMS error in baseline length and so on, and A_H, A_B and so on are the scale factors given by [8]

$$A_r = \frac{\partial h}{\partial r} + \frac{\partial h}{\partial \theta}\frac{\partial \theta}{\partial r} = -\frac{\sin(\gamma+\nu)\left(\frac{\Delta r^2}{2Br} - \frac{B}{2r}\right)}{K} + \cos(\gamma+\nu), \tag{2.8}$$

$$A_B = \frac{\partial h}{\partial \nu}\frac{\partial \nu}{\partial B} = \frac{\sin(\gamma+\nu)\left(\frac{1}{2} + \frac{(r+\Delta r)^2 - r^2}{2B^2}\right)}{K}, \tag{2.9}$$

$$A_H = \frac{\partial h}{\partial H} = 1, \tag{2.10}$$

$$A_\gamma = \frac{\partial h}{\partial \gamma} = -r\sin(\gamma+\nu), \tag{2.11}$$

$$A_\phi = \frac{\partial h}{\partial \nu}\frac{\partial \nu}{\partial \Delta r}\frac{\partial \Delta r}{\partial \phi} = \frac{\sin(\gamma+\nu)(r+\Delta r)}{2\pi BK}, \tag{2.12}$$

$$A_\lambda = \frac{\partial h}{\partial \nu}\frac{\partial \nu}{\partial \Delta r}\frac{\partial \Delta r}{\partial \lambda} = \frac{\sin(\gamma+\nu)(r+\Delta r)\phi}{2\pi BK}. \tag{2.13}$$

Here,

$$K = \sqrt{1 - \left(\frac{B^2 + r^2 - (r+\Delta r)^2}{2Br}\right)}. \tag{2.14}$$

It can be seen that as the baseline increases, the height error decreases, but sensitivity (and geometric decorrelation), and ambiguity increase. In terms of the baseline angle and ground slope, as the baseline aligns to the cross-track slope, error decreases, but sensitivity (and geometric decorrelation), and ambiguity increase. It is this trade-off along with the choice of resolution lengths in cross-track and along-track planes, that influence the choice of interferometric parameters. The following chapter uses the

above discussion on mapping, resolution, sensitivity and accuracy to arrive at these choices for a prototype rooftop instrument.

CHAPTER 3

CONFIGURATION OF THE INTERFEROMETER

This chapter discusses the configuration of the interferometer in terms of geometry and radar hardware. The section describing the geometric configuration applies the sensitivity, resolution, and error analysis concepts from Chapter 2 to arrive at design values and expected height error estimates for the special case of the rooftop instrument. The section on hardware configuration describes the radar system design in terms of the technology used and critical specifications of the various hardware functional blocks of the radar.

3.1 Geometric configuration

The parameters defining the geometry of the interferometer are deployment height (H), baseline length (B), baseline angle (γ), look angle (θ), antenna azimuth and elevation beamwidths (Φ_{az} and Φ_{el}), range resolution (δ_r), ground resolutions in azimuth and elevation (δ_{az} and δ_{el}), and cross-track and along-track slopes (τ_c and τ_a). The three main factors limiting the possible range of values permissible for these variables are (i) feasibility of hardware design and deployment, (ii) maximum allowable amount of geometric decorrelation, and (iii) maximum allowable vertical height error.

For a fixed baseline and a given target, the amount of geometric decorrelation increases with decreasing deployment height. This makes the minimum deployment height, H_{min} a critical declarative in the geometric configuration. Owing to feasibility and availability of a good view of favorable targets, the Lederle Graduate Research Center (LGRT) at the University of Massachusetts, Amherst was chosen as the first

deployment site for the prototype instrument. Further deployments of the instrument are desired to be on either cliffs or airborne platforms. This reduces the minimal deployable height of the instrument to the height of LGRT which was measured by a stereoscope to be 65m.

The radar being bandwidth limited in elevation, a wide swath is desirable. It is shown later that for acceptable height error, look angles of at least 20° are desirable. Look angles exceeding 70° are not used due to high path losses. This requires the elevation beamwidth of the antenna, Φ_{el} to be less than 50°. Radar bandwidth is influenced by the need to maintain a desired cross-track resolution for this range of look angles. In light of (2.3), the worst cross-track ground resolution is at the lowest look angle, 20°. A worst case cross-track resolution of at least 5m is desirable for the kind of terrain the prototype interferometer will map. Using these limits and (2.3), the required radar bandwidth can be shown to be about 100 MHz. It is shown later (see Figure 3.1) that this value of cross-track resolution gives an acceptable amount of geometric decorrelation.

Unlike elevation, the radar is beam-limited in azimuth requiring a narrow azimuth swath. Azimuth resolution reaches its worst case at the far range look angle of 70°. Using (2.4), a worst case azimuth ground resolution of 5m from a deployment height of 65m requires an azimuth beamwidth, Φ_{az} of at most 1.5°.

The last set of parameters to be given values are the acceptable ground slopes and the baseline. Equation 2.9 suggests the use of a long baseline to minimize height error, while (2.5) advocates a smaller baseline to minimize geometric decorrelation. This trade-off depends on the cross-track slope and deployment height that vary depending on the deployment site. The same trade-off between height error and baseline decorrelation exists in choosing the baseline angle in that, as the baseline is made parallel to the cross-track slope, geometric decorrelation increases and height error decreases, and as the baseline is made perpendicular to the cross-track slope,

geometric decorrelation decreases and height error increases. Making these trade-offs depending on the target at the deployment site requires a variable baseline length and angle. This variability is required only when the deployment site changes, and there is no real need of automation. The range of feasible and permitted values for the baseline length and angle are however design values to be declared. Baseline angles below 0° and above 90° are not feasible due to blockage of one antenna by the other, and it is desirable to have an antenna mounting system capable of varying the baseline angle between 0° and 90°. The smallest possible baseline length is dictated by the dimensions of the antenna itself and is about 20mm (see Chapter 4). The critical baseline[†] for the rooftop deployment looking at a wide range of cross-track slopes at look angles between 20° and 70° is of the order of a few hundred millimeters. Based on these numbers, the feasible range of baseline lengths is between 20mm and 200mm.

Table 3.1 summarizes the choice of geometric parameters of the instrument, and Figure 3.1 depicts the extent of geometric decorrelation for these parameters.

Table 3.1. Interferometric parameters for the LGRC deployment

Parameter	**Value**
Minimum deployment height	65m
Baseline length	20mm to 200mm
Baseline angle	0° to 90°
Range resolution	1.5m
Antenna 3dB azimuth beamwidth	1°
Antenna 3dB elevation beamwidth	45°
Worst case ground resolution in elevation plane on flat ground	4.4m at $\theta = 20°$
Worst case ground resolution in azimuth plane on flat ground	5m at $\theta = 70°$

[†]Critical baseline is that value of the baseline length that gives rise to a 2π change in interferometric phase within one resolution pixel.

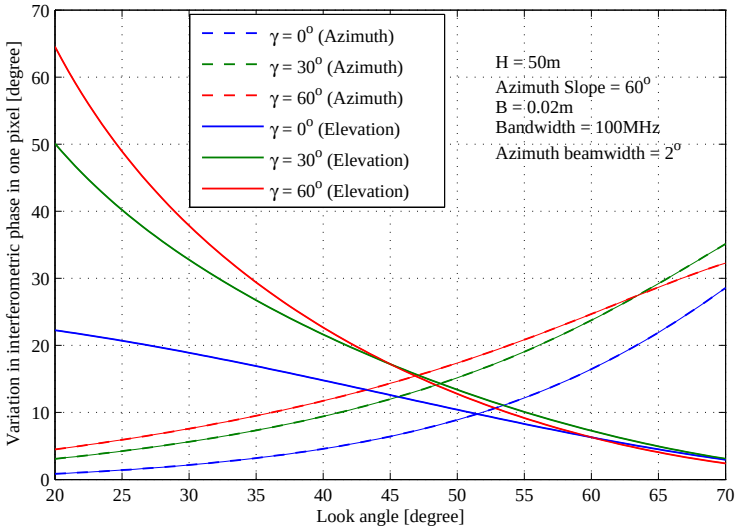

Figure 3.1. Variation of interferometric phase in azimuth (broken line) and elevation (solid line) within a pixel

3.2 Hardware configuration

This section addresses the issue of identifying the different functional blocks that make up the hardware of the prototype interferometer and the specifications of these blocks which are critical to system performance.

The center frequency of the radar within the Ka-band is chosen in accordance to the recommendations in the report on specifications of the Wide Swath Ocean Altimeter (WSOA) as 34.945GHz. Such a high frequency requires two stages of downconversion and upconversion to ease the design of image-reject and LO isolation filters (discussed later). The intermediate frequency is chosen in accordance to the WSOA specifications as 1.245GHz. The output of the RF front end is centered at 55 MHz with a bandwidth of 100 MHz as mentioned earlier. In order to reduce the peak transmit power, this bandwidth is achieved by pulse compression using a linear frequency chirp. The Local oscillators (LOs) for the two stages of downconversion are at 33.7GHz and 1.3GHz. The second stage of downconversion is the same as the

one employed in the UMass Ku-band interferometer [7] facilitating interchangeability and ease in design and evaluation.

The hardware blocks used to accomplish these upconversion and downconversion operations are shown in Figure 3.2. The baseband electronics comprises of a digital system having signal generation, RF data acquisition, telemetry data acquisition, radar timing, and control capabilities. (i) Signal generation involves a Direct Digital Synthesis (DDS) of the frequency modulated chirp into a high speed digital to analog converter. (ii) RF data acquisition is accomplished by sampling the two channels of the radar receiver front end using a high speed (few hundred Megabits per second) analog to digital converter. (iii) Telemetry data involving bias levels, downconverter component temperatures and power levels are sampled by a low speed (several kilobits per second) analog to digital converter which also manages the radar timing and control signal generation. Each of the three functionalities mentioned above is facilitated by a separate module connected to a common PXI-express [†] bus housed in a cage called the PXIe chassis. These modules are programmed and controlled by a computer controller on the bus. This controller also provides the user interface and real time signal processing capabilities. The RF and telemetry data so acquired are streamed in real time to a RAID (Redundant Array of Inexpensive Disks) through a RAID controller module.

The RF upconversion and downconversion are accomplished using Printed Circuit Board (PCB) technology to minimize cost, size, weight, and to achieve reliability through a high level of circuit integration. As mentioned earlier, the upconversion and downconversion are done in two stages. The upconverter accepts the baseband frequency chirp from the DDS module, and performs the two stages of upconversion on a single PCB. The final stage power amplifier is a waveguide amplifier since the re-

[†]PXI express specifications can be found at http://www.pxisa.org/Specifications.html

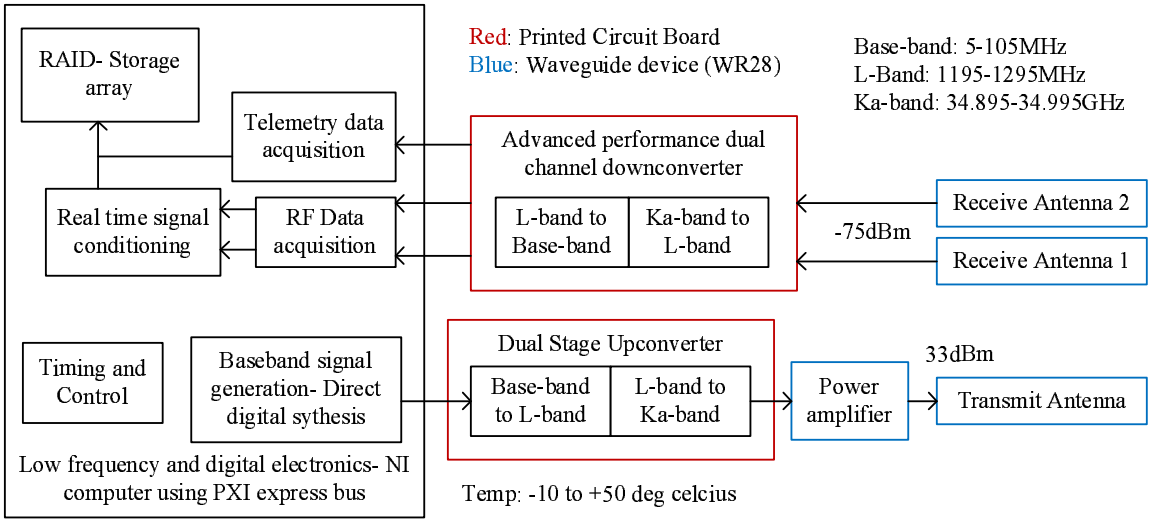

Figure 3.2. Hardware block schematic of the interferometer

quired transmit power of 1Watt poses heat dissipation problems in bare dies mounted on PCBs. The downconverter uses the same components as the upconverter, and the two stages of downconversion are designed into different PCBs to provide redundancy and interchangeability with the UMass Ku-band dual downconverter [7]. The downconverter also has temperature, bias voltage and current, and power sensors along with low frequency analog to digital converters integrated into the PCB. The telemetry data from these analog to digital converters are read out by the digital I/O lines on the low frequency data acquisition module in the PXIe system. The downconverted baseband data is sampled by the high speed RF data acquisition module in the PXIe system. Both the upconverter and downconverter PCBs are four-layered. The signal layers from top to bottom are used for RF signal, ground, bias supply and telemetry data respectively. The top dielectric propagating RF signals is RT Duroid 6002. All other dielectric layers are standard FR-4 (Flame Retardant-4). An exception is the L-band to baseband downconverter on which all dielectric layers are standard FR-4.

The antennas for the interferometer must be rugged due to the future possibility of an aircraft deployment. As discussed earlier, they should generate a fan beam with

3dB beamwidths of less than 2° and 50° respectively. Although microstrip antennas are relatively easy to design, high dielectric losses at Ka-band discourage their use due to their long and lossy feed network. A slotted-waveguide configuration was chosen as it is rugged and low loss, and is an ideal technology for these requirements. To eliminate a potential trouble in using transmit/receive switches having unpredictable insertion phase, three separate antennas, one for transmit and two receive were manufactured.

The downconverter, transmitter, and antennas are discussed in detail in Chapter 4.

CHAPTER 4

RADAR HARDWARE DESIGN

Chapter 3 presented the architecture and primary functions of the various radar hardware blocks. This chapter discusses the detailed design and specifications of the radar downconverter, transmitter, and antennas. The downconverter, being the most critical part of the radar, is discussed in greater detail.

4.1 Dual Downconverter- DDC

The design and evaluation of the DDC was supported by an Advanced Component Technologies (ACT) grant from NASA's Earth Science Technology Office (ESTO). The performance specifications of the DDC were charted out by the Wide Swath Ocean Altimeter (WSOA) team. The DDC was designed for a radar bandwidth of 100 MHz instead of the 20 MHz recommended by the WSOA specification document to adapt the interferometer for a rooftop deployment. Nevertheless, the DDC can be reverted back to the original WSOA specifications by replacing the baseband filters. These two sets of specifications are shown in Table 4.1 separately under DDC ACT and DDC UMass columns.

Figures 4.1 and 4.8 show the hardware block diagram of Ka-band to L-band downconverter and L-band to baseband downconverter PCBs designed for these specifications[†].

[†]Datasheets of all components used in the two PCBs can be found in [5].

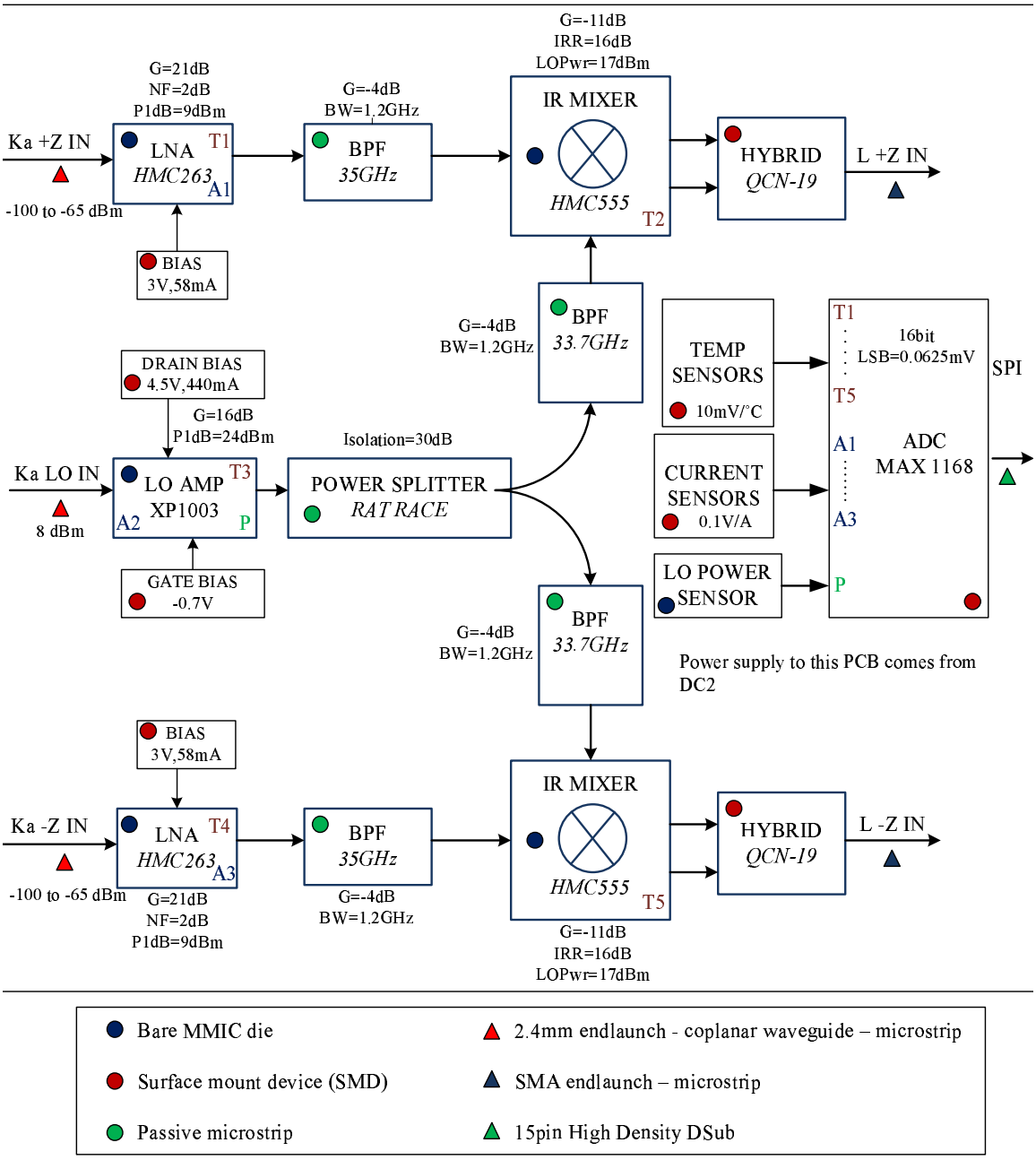

Figure 4.1. Block schematic of the Ka-band to L-band downconverter PCB (DC1)

Table 4.1. System requirements for the DDC

Design parameter	**DDC ACT**	**DDC UMass**
Signal bandwidth	20 MHz	100-120 MHz
Effective noise bandwidth	<30 MHz	<140 MHz
Input frequency range	34.975-34.995GHz	34.895-34.995GHz
Operating temperature	$-10°$ to $-50°$	$-10°$ to $-50°$
Noise figure	<4.5dB	<4.5dB
Output frequency range	5-25 MHz	5-105 MHz
Inter-channel isolation	>80dB	>80dB
Input/Output VSWR	<1.5:1	< 1.5:1
Inter-channel phase stability	< 0.05°RMS over BW	< 0.15°RMS over BW
Amplitude variation	2dB over BW	2dB over BW
Input signal range	-100 to -65 dBm	-100 to -65 dBm
DDC end to end gain	65 to 70dB	65 to 70dB
Image rejection	>30dB	>30dB

4.1.1 Ka-band to L-band downconverter

The Ka-band part of the circuitry, owing to its high operating frequency requires attention to minor design details and fabrication precision. This is aggravated by the non-availability of surface-mount components owing to high package parasitics forcing the integration of bare semiconductor dies (MMIC) into the PCB. Figure 4.2 shows the close up of one such MMIC- the low noise amplifier with a chip capacitor. The DC bias and the RF lines are connected to the MMIC through delicate gold bondwires that are about one-thousandth of an inch in diameter.

Minimizing cost, design time, and risk in such a situation contsraints the Ka-band to L-band downconversion to be accomplished with a bare-minimum of components. The downconverter circuitry can be functionally divided into three categories. They are (i) the RF downconversion chain, (ii) the LO distribution chain, and (iii) the telemetry and bias circuitry. A description of the important components in the three circuits and their design follows.

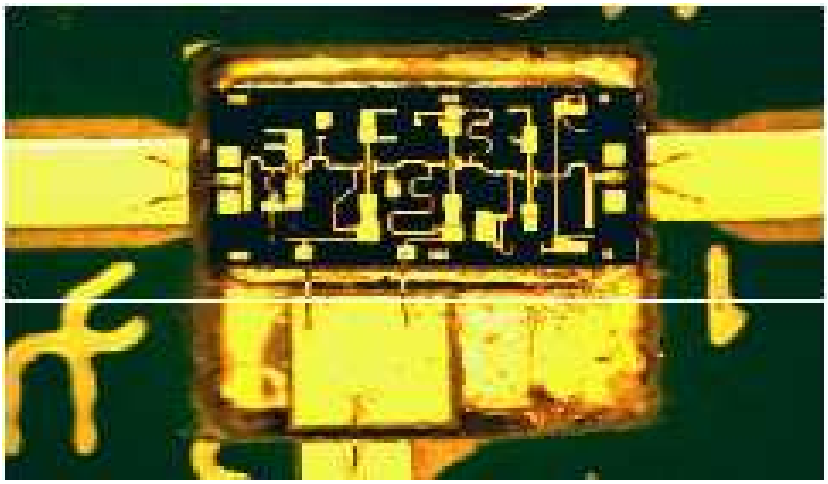

Figure 4.2. Picture of the Ka-band front end LNA showing delicate gold wire bonds

4.1.1.1 RF Downconversion

To obtain a good noise figure, the first device on the RF chain is the Low Noise Amplifier (LNA). The LNA used is manufactured by Hittite Corp with part number HMC263. It is a Gallium Arsenide (GaAs) based MMIC having a gain of 22dB and a noise figure of 2dB at 35GHz. It will be seen later that this gain and noise figure suffice in meeting the overall DDC noise figure requirement given in Table 4.1. The LNA has an absolute maximum RF input of -5dBm. Since these power levels are not expected at the receiver input, and to minimize the receiver noise-figure no input power protection device has been employed. This also avoids a potentially bigger problem posed by the uncharacterized and unpredictable phase response of such devices, leaving the LNAs safety in the hands of the radar operator.

The next component in the RF chain is the RF filter. Again, due to the non-availability of lumped elements at 35GHz, microstrip technology is used for this filter. Due to the small fractional bandwidth of the received signal at Ka-band (about 0.3%) this filter cannot be used as a channel select filter. The low intermediate frequency (L-band) puts the image frequency for the first stage of downconversion at a distance of 2.49GHz from the RF frequency. Using this filter as an image-reject filter to achieve an

image-rejection of 30dB would result in a high order filter having high pass-band loss and spurious radiation. In light of all this, the RF front end filter was designed to aid partially in image-rejection while rejecting the out of band interference from entering the rest of the downconverter. Microstrip coupled line filters were chosen because of the vast design resources available [1] and their small PCB footprint size to filter order ratio. Based on a trade-off study between image-rejection and pass-band attenuation, a 4-section coupled line filter was designed[†]. A matter of concern in the RF filter and the LO filter (discussed later) design was that the drift in filter response due to the substrate dielectric constant variation between batches and due to the fabrication process were large enough to push the stop-band rejection and pass-band insertion loss out of acceptable design limits. To meet the design specification accurately, five prototype filters were designed with varying coupled line lengths and the one matching the required specifications best was chosen. A plot of the $\mathcal{S}$-parameters of the prototype filters is shown in Figure 4.3. A suitable RF filter has its pass-band around 35GHz, and is shown in bold lines. The other filter in bold lines having its pass-band around 33.7GHz is the LO filter which will be discussed later.

To augment the image-rejection provided by the RF filter an image-reject mixer with an external IF hybrid was chosen for the Ka-band to L-band downconversion. This mixer is a GaAs MMIC manufactured by Hittite Corp bearing part number HMC555. It is driven by an LO of about 17dBm, and has a conversion loss of about 11dB. The mixer requires an external surface mount IF hybrid which is the last component on the Ka-band to L-band downconversion chain.

4.1.1.2 LO distribution

The second functional chain on the Ka-band to L-band downconverter is the LO distribution network. Two main design concerns in providing the LO for the two RF

[†]Details of the filter design are omitted for brevity

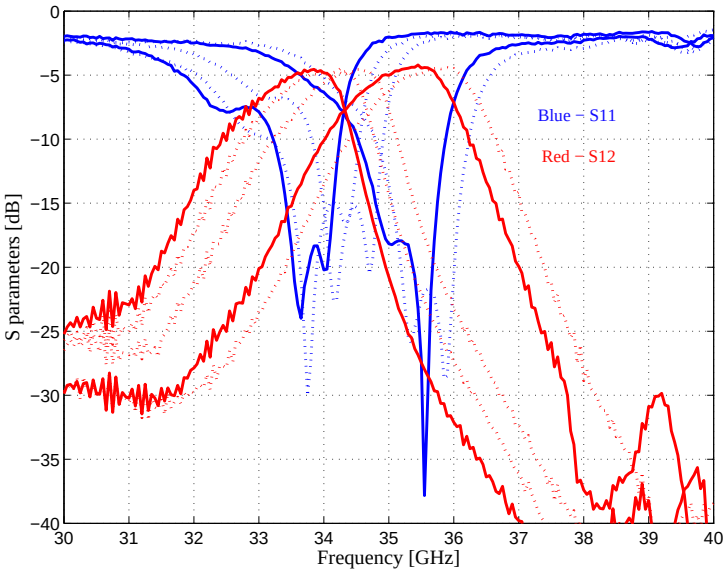

Figure 4.3. $\mathcal{S}$-parameters of the RF filter prototypes

downconversion channels are (i) meeting the high power requirement of the image-reject mixers, and (ii) avoiding conductive coupling of one interferometric channel into the other through the LO distribution chain. Most commercially available oscillators supply about 13dBm of power. To meet the power specifications of the mixers a medium power LO amplifier is required. The XP1003 manufactured by Mimix Broadband is used as the LO amplifier. This GaAs MMIC amplifier has a gain of 16dB, and an output 1dB compression point of 24dBm guaranteeing sufficient LO drive for the mixers. The RF to LO isolation of the image-reject mixers used do not suffice for the tall order of inter-channel isolation (80dB) specified. This requires LO filters that can pass the LO but reject the RF on the LO supply lines. Figure 4.4 shows this signal leakage path on which filtering is required with the design values for the required RF rejection from the LO filters and the isolation on the rat-race hybrid used to split the LO power into the two interferometric channels. For reasons mentioned before, a parallel coupled line filter was used as the technology for the LO filter. The required value of RF insertion loss from these filters as shown in Figure 4.4 needs a four stage coupled line filter. Like the RF filter, prototypes for the LO filter

were fabricated with varying coupled line lengths and the best one chosen. A plot of the $\mathcal{S}$-parameters of the prototype filters is given in Figure 4.3, and the filter shown in bold lines centered with pass-band centered around 33.7GHz is the the chosen LO filter.

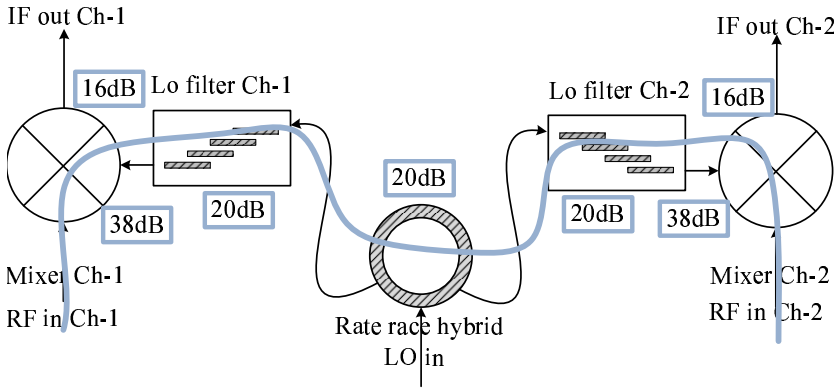

Figure 4.4. Primary path for the inter-channel conductive leakage in the Ka-band to L-band downconverter PCB and contributors to the inter-channel isolation

4.1.1.3 Telemetry and bias

Bias circuitry includes the voltage regulation and distribution for the active RF components in the downconversion and LO distribution chain. Telemetry circuitry includes measurement of (i) temperatures at the active RF components on the board, (ii) bias conditions for the RF components, and (iii) LO power level monitoring. Both PCBs of the DDC work on a single 15V DC input on the L-band to baseband downconversion board. The Ka-band to L-band board works off a regulated 6V DC line from the L-band to baseband board. Figure 4.5 shows the bias network with the power consumption on each bias line.

To avoid switching harmonics contaminating the RF signals, all voltage regulators but for the positive to negative voltage converters are linear regulators as opposed to switching regulators. This comes with an additional cost of having a low voltage regulation efficiency due to thermal dissipation in the linear regulators. Nevertheless,

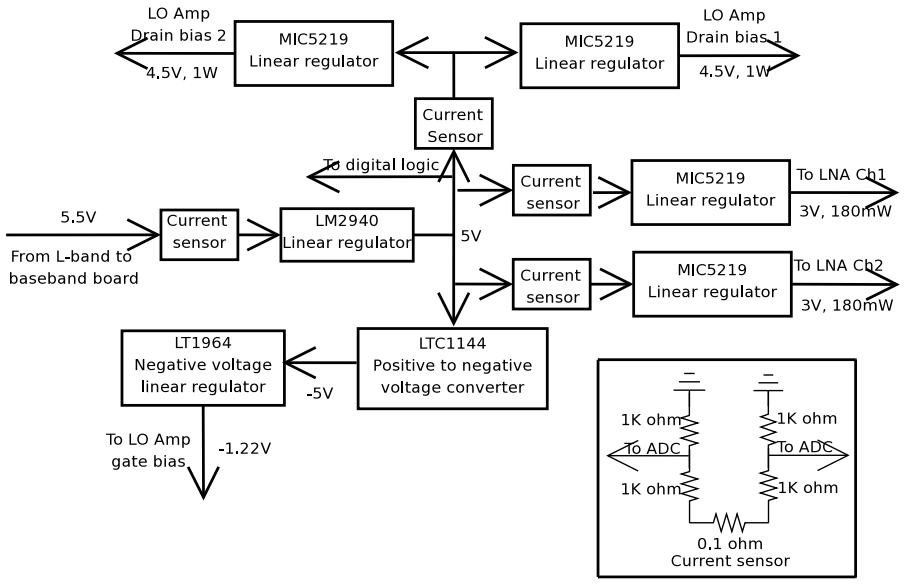

Figure 4.5. Block schematic of the Ka-band to L-band downconverter's bias circuitry

lumped LC filters have been placed on all bias lines to reject switching harmonics from the master switching regulator on the L-band to baseband downconverter board. Apart from rejecting witching harmonics, the drain bias regulators for the XP1003 are delayed from the gate bias using simple RC delay lines to avoid damaging drain inrush currents.

The telemetry circuit (see Figure 4.6) includes various sensors and a low speed Analog to Digital Converter (ADC). The sensors include (i) temperature sensors, (ii) current sensors, and (iii) power sensors. The temperature sensors used are integrated circuit surface mount devices with output voltage proportional to temperature. This voltage is sampled by the ADC. Current sensing is accomplished by sampling the voltage on either sides of a small precision resistance in series with the line. LO power sensing is done by an integrated power sensor on the LO amplifier that drives a voltage which is a function of the amplifier output power.

Figure 4.7 shows a picture of the Ka-band to L-band downconverter PCB housed in a custom made chassis. The same chassis also houses the L-band to baseband

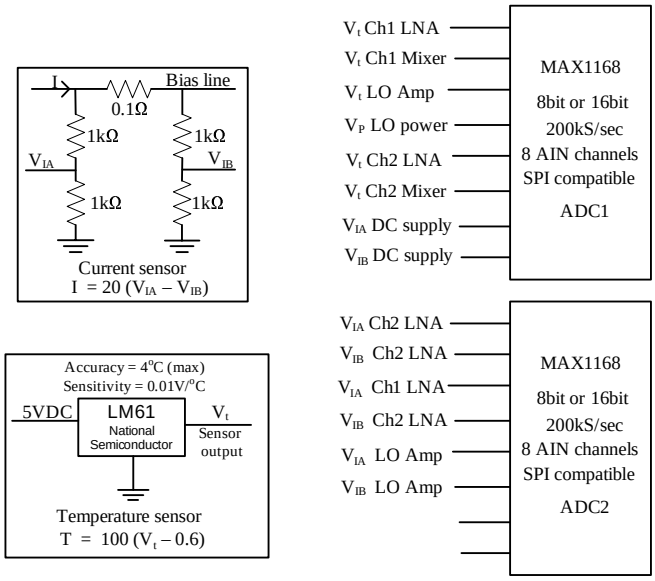

Figure 4.6. Block schematic of the Ka-band to L-band downconverter's telemetry circuit

downconverter (not shown in picture). The lid of the chassis has been taken off. The filter cavities on one of the downconversion channels have also been taken off to reveal the RF and LO coupled line filters.

4.1.2 L-band to baseband downconverter

The first stage of downconversion is achieved with bare minimum requirements. Owing to the relatively lower cost and greater ease in finding suitable surface mount components at L-band and baseband, the L-band to baseband downconverter PCB is responsible for noise filtering, RF power monitoring, and most of the system end-to-end gain. Figure 4.8 shows the block schematic of the L-band to baseband downconverter. This PCB is the same as the one developed for the UMass Ku-band interferometer, and its hardware description may be found in [7]. Nevertheless, a brief description of the RF chain, LO distribution chain, telemetry, and bias subsystems on this PCB is included for completeness.

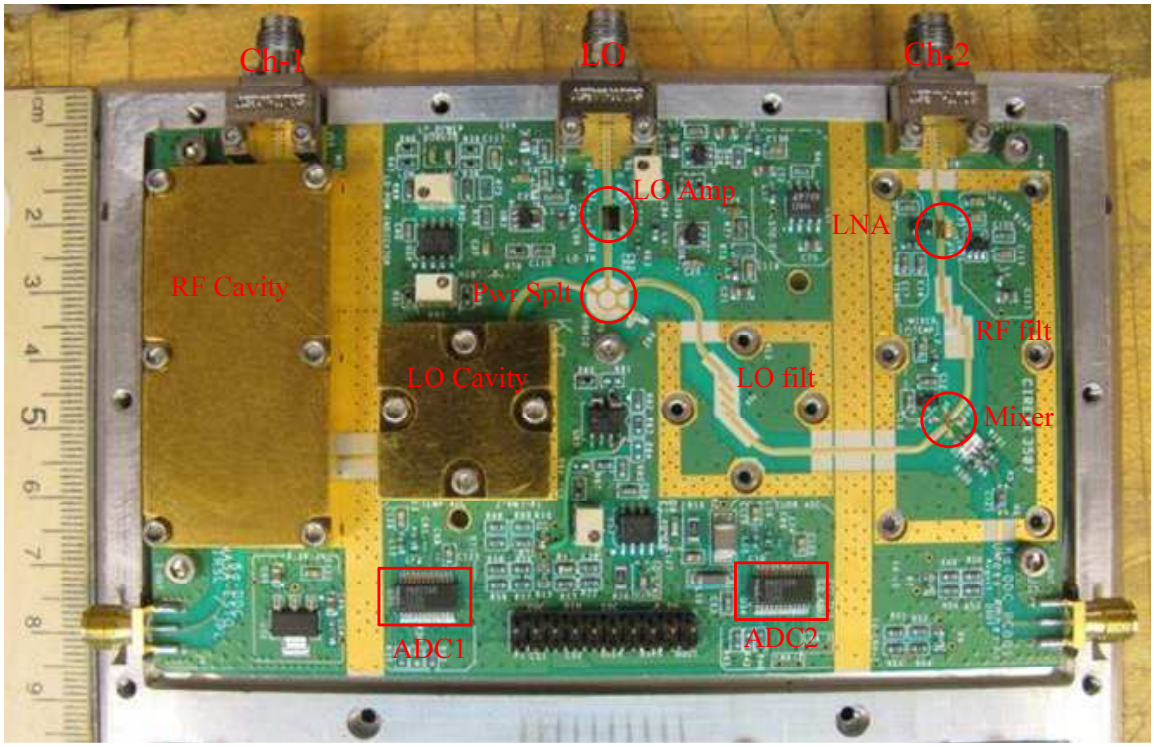

Figure 4.7. Picture of the Ka-band to L-band downconverter PCB

4.1.2.1 RF downconversion

The first component in the RF downconversion chain is the IF amplifier which boosts the RF power level into the dynamic range of the RF power detector employed. The component providing this amplification is the ECG005, manufactured by TriQuint Semiconductor. It has a gain of 22dB, noise figure of 3.3dB and an output 1dB compression point of 18dBm. The next component in the chain is the IF filter (also referred to as the L-band filter) that is used as an image-reject filter for the second downconversion stage. The specified $\mathcal{S}$- parameters of the IF filter are shown in Figure 4.9. Due to the increased radar bandwidth of 100 MHz, image-rejection with this 5-pole filter is just 20dB at mid-band. However, a 5-pole filter can easily provide the required image-rejection of 30dB if the WSOA specified bandwidth of 20 MHz is used. The next component in the downconverter chain is a a coupler which couples a small part of the RF signal into an RF power detector to monitor the

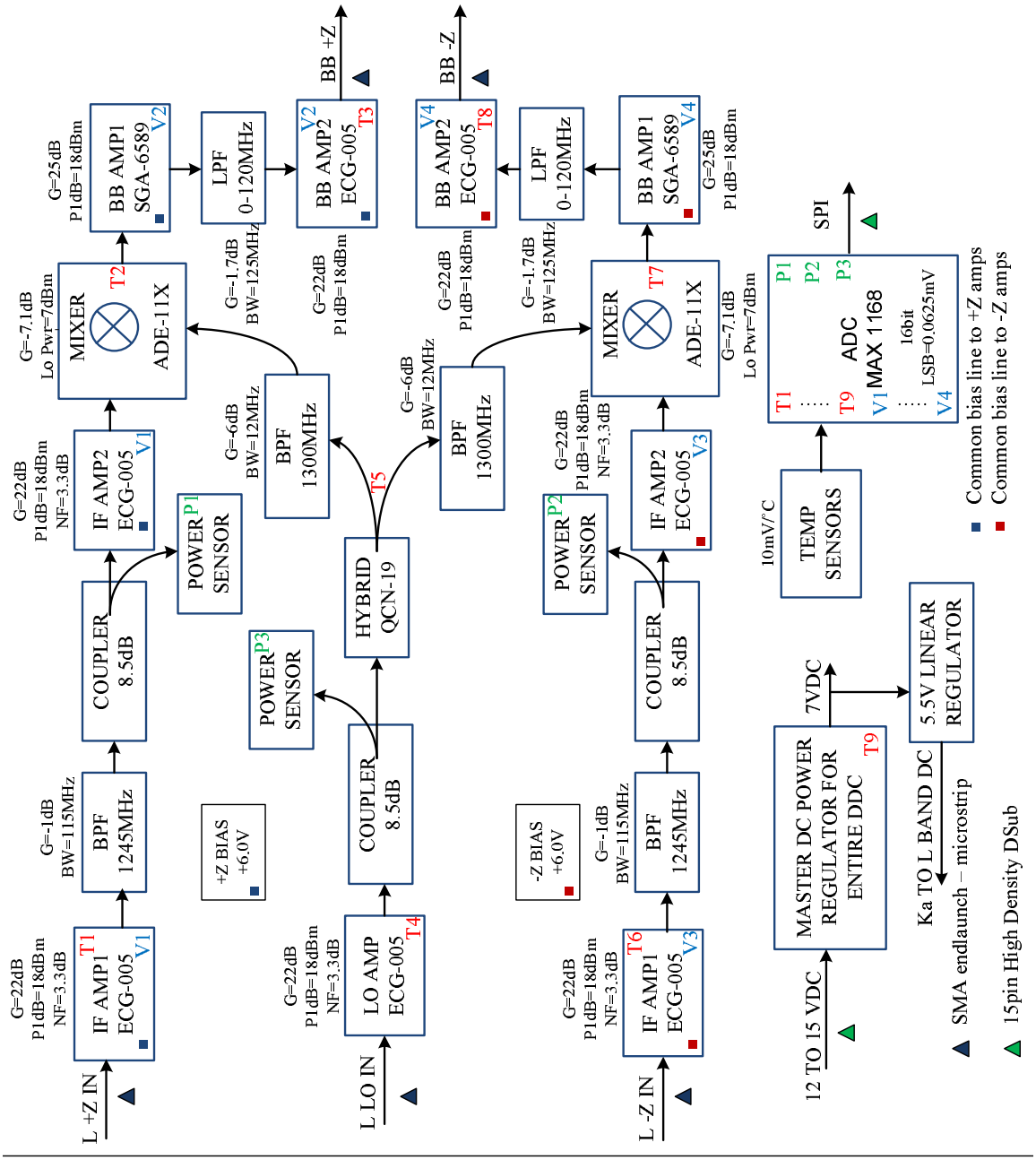

Figure 4.8. Block schematic of the L-band to base-band downconverter PCB (DC2)

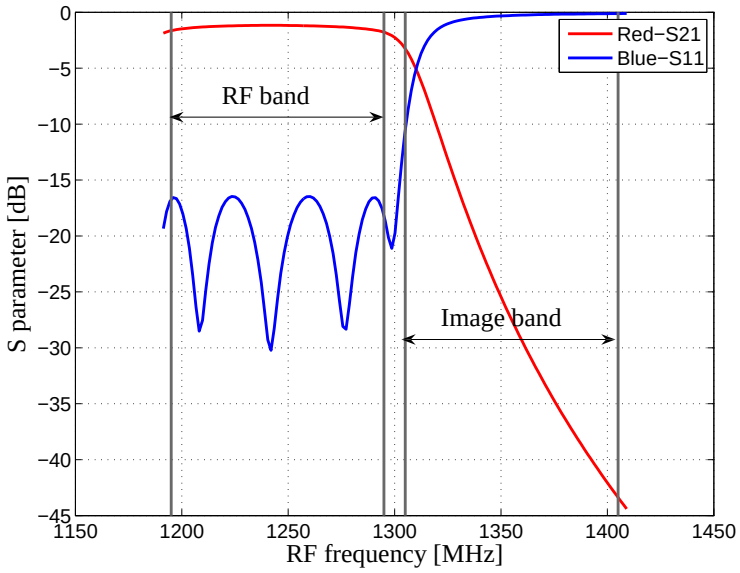

Figure 4.9. Company specified L-band RF filter response

radar received power through the telemetry subsystem. This coupler is followed by another ECG005 amplifier used as an IF gain block. This is followed by the L-band to baseband mixer. Due to the non-availability of hybrids at baseband owing to a high fractional bandwidth (100 MHz centered at 55 MHz), image-reject mixing is not possible, and an ordinary doubly-balanced mixer is used. This mixer bears the part number ADE-11X, and is manufactured by Minicircuits. It requires an LO power of 7dBm, and has a conversion loss of about 7dBm. Another ECG005 gain block follows this mixer. This is followed by the baseband low pass filter which rejects the unwanted mixing products and provides noise bandwidth filtering. This filter has a cut off at 120 MHz rather than 105 MHz to save the pass-band from large insertion phase variations at the band edges. Figure 4.10 shows the measured $\mathcal{S}$-parameters of the baseband low pass filter.

4.1.2.2 LO distribution

The LO distribution chain on the L-band to baseband downconverter circuit has the same architecture as the one on the Ka-band to L-band downconverter circuit.

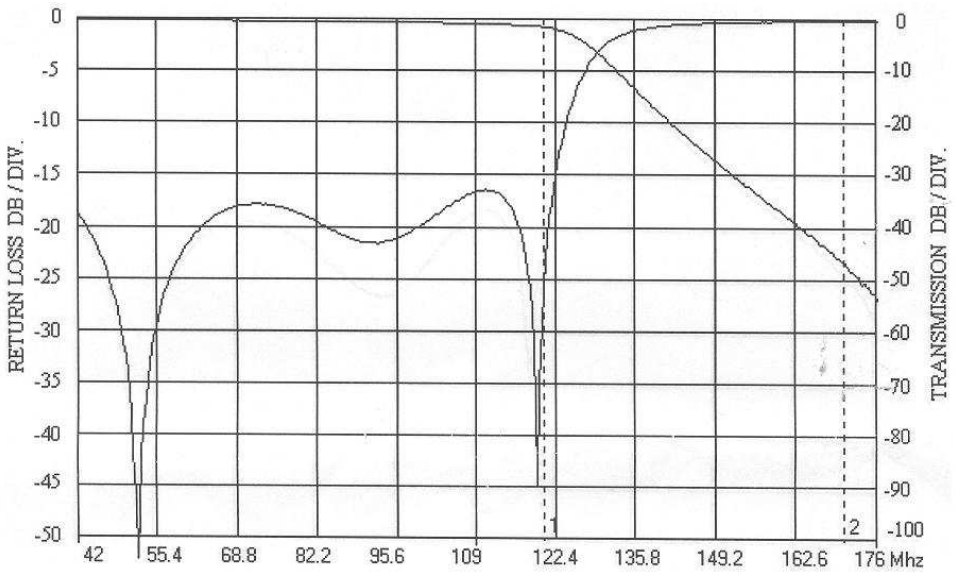

Figure 4.10. Measured baseband low pass filter response

The LO amplifier is the ECG005 from TriQuint Semiconductor. Since this amplifier does not have an in-built power detector, the amplified LO is coupled off by an 8.5dB coupler into a surface mount IC power detector. A surface mount hybrid follows the coupler, and splits the LO into the two LO filters used to improve inter-channel isolation. The $\mathcal{S}$-parameters of the LO filter are plotted in Figure 4.11.

A potential inter-channel leakage path exists through the LO distribution. This leakage path is the same as the one in the Ka-band to L-band downconverter, and is depicted in Figure 4.4. The ensuing conductive leakage is well within the 80dB requirement because (i) the specified RF to LO isolation of the mixer ADE-11X is about 35dB, (ii) the midband RF rejection from the LO filters is about 55dB, and (iii) the midband isolation in the hybrid is about 20dB.

4.1.2.3 Telemetry and bias

Figure 4.12 shows the block schematic and the DC power budget of the L-band to baseband downconverter bias circuitry. The power supply for the whole dual downconverter comes in at the L-band to baseband downconverter board into a master

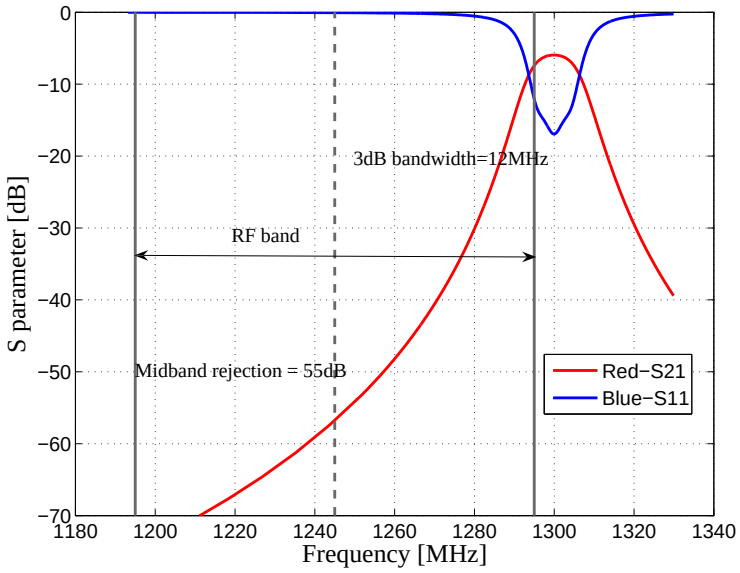

Figure 4.11. Company specified L-band LO filter response

power regulator. This regulator is a switching regulator, and converts an input in the range of 12V to 15V to an output at 7V. Despite the presence of LCπ filters on every bias line, switching harmonics from this regulator enter the RF lines, although not on a prohibitive magnitude. Nevertheless, it is possible to bypass this regulator, and supply the dual downconverter with a regulated clean 7VDC. This is accomplished by merely shutting off the regulator by driving a digital logic line low and placing a 0Ω resistor as a jumper. The output of the master power regulator feeds different linear regulators. These regulators bias the active components and provide power for the digital logic circuits and the Ka-band to L-band downconverter PCB.

Figure 4.13 shows the block schematic of the L-band to baseband telemetry subsystem. The telemetry circuitry is similar in architecture the the one on the Ka-band to L-band downconverter. The only difference being the log power detection to monitor the RF and LO power levels. This is accomplished by the AD8317 log power detector that can detect instantaneous pulse power. The output of this detector is also passed through an opamp buffer, which due to its low bandwidth acts as an integrator and gives out the average power.

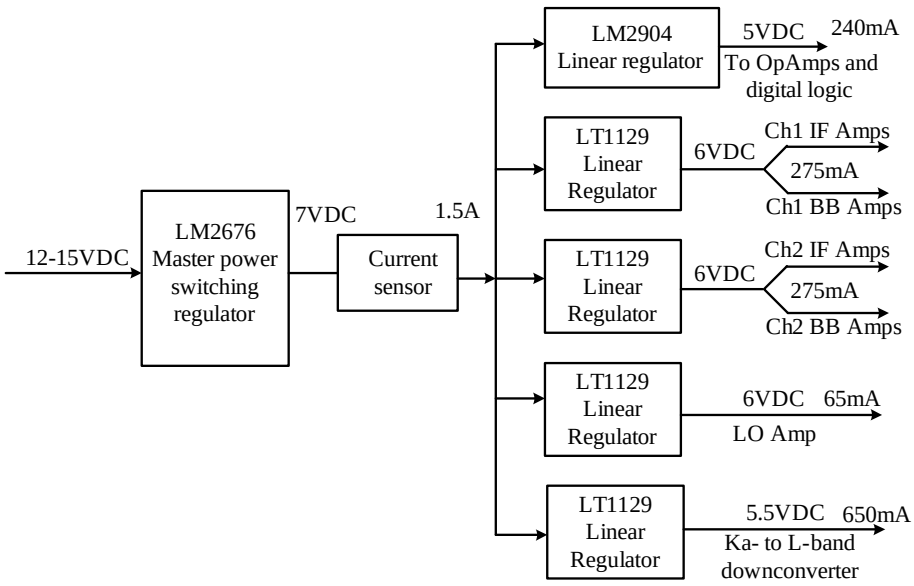

Figure 4.12. Block schematic of the L-band to baseband downconverter's bias circuitry

The SPI interface lines on the ADCs of both the PCBs lie on a common bus with chip select lines to choose between the ADCs. These lines along with the power supply are passed outside of the dual downconverter through a 15pin D-Sub connector.

Figure 4.14 shows a picture[†] of the L-band to baseband downconverter PCB housed in the custom chassis. Figure 4.15 shows both the Ka-band and L-band downconverter boards housed in the chassis with the chassis lid taken off.

4.2 Transmitter

Figure 4.16 shows the block schematic of the Ka-band dual upconverter (transmitter). This circuit, like the downconverter, is a four-layered PCB. The four layers carry RF, ground, telemetry, and power signals. The transmitter however, does not have telemetry circuitry and the telemetry layer is used minimally. Following is a brief description of the RF signal path. Since the transmitter has the same active

[†]The L-band image reject filter has been de-soldered and repleced with a co-axial line in this picture.

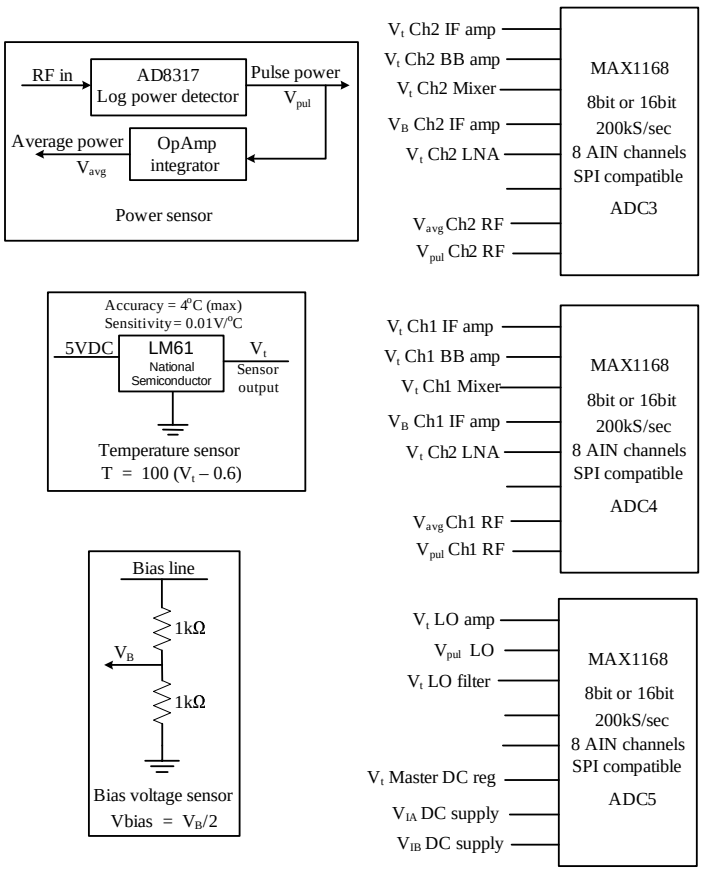

Figure 4.13. Block schematic of the L-band to baseband downconverter's telemetry circuitry

devices as the downconverter, it has a similar bias circuitry. Owing to this, details of the bias circuitry are omitted for brevity.

The baseband signal generated by a direct digital synthesis is first amplified by the ECG005 amplifier. There is a provision for this amplifier to be bypassed in case the direct digital synthesis provides enough power. The signal is then passed through the baseband low-pass filter to reject possible out of band interference and noise. It then goes through the ADE-11X mixer for the first stage of upconversion. The IF filter then rejects the upper side-band and allows the lower side-band of upconversion to pass. The information at baseband has now been upconverted to L-band. This L-band signal is then amplified by another ECG005 amplifier stage. The signal then

Figure 4.14. Picture of the L-band to baseband downconverter PCB

goes through an RF switch that, depending on digital inputs, directs the RF energy either into the transmit chain or into a matched 50Ω load. This switch is opened during transmit and closed on receive. Ideally it would be desirable to employ the transmit switch at Ka-band before the transmit antenna. Switches at Ka-band are expensive, and a Ka-band waveguide switch can always be integrated with the system if required. The next operation in the transmit chain is the second upconversion stage employing an image reject mixer configuration using the HMC555 and an external L-band hybrid. The image-reject mixing circuitry has been configured to give only the upper side-band. This Ka-band upper side-band is then amplified by a HMC283LM1 pre-amplifier (manufactured by Hittite Co.) and later by a waveguide power amplifier before being transmitted. The HMC283LM1 is a surface mount Ka-band amplifier with a gain of 21dB and a saturated output power of 21dBm. The waveguide power

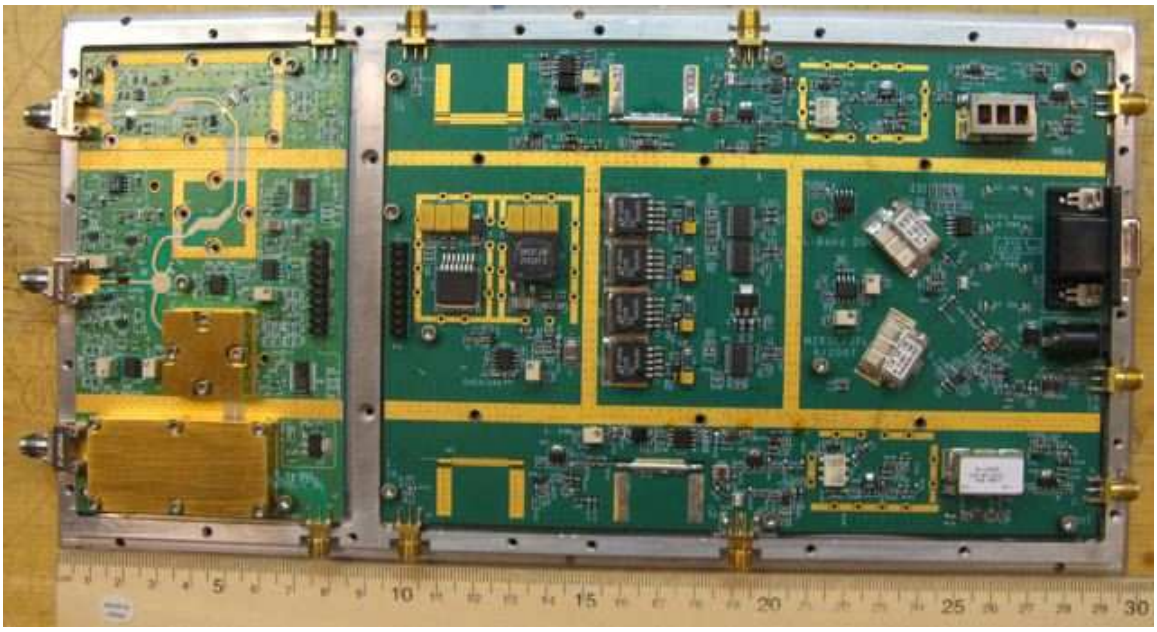

Figure 4.15. Picture of the Ka-band dual-downconverter (DDC) in its custom chassis

amplifier is the AMP-28-01090 manufactured by Millitech Inc. and has a saturated output power of 1W.

The bandpass characteristics of the transmitter are not critical in the operation of the interferometer since interferometry basically involves a differential measurement, and the variations in the transmit signal is common to both channels. Owing to this, the bandpass characteristics and lab evaluation of the transmitter has been omitted from Chapter 5. Moreover, the transmitter for future airborne deployments will have a different architecture due to high transmit power requirements, and documentation of the present transmitter bandpass characteristics will not necessarily serve as a reference for future airborne and spaceborne missions.

4.3 Antennas

As discussed in Chapter 3, the antennas for the interferometer have a slotted-waveguide configuration. A slotted waveguide antenna can have different slot con-

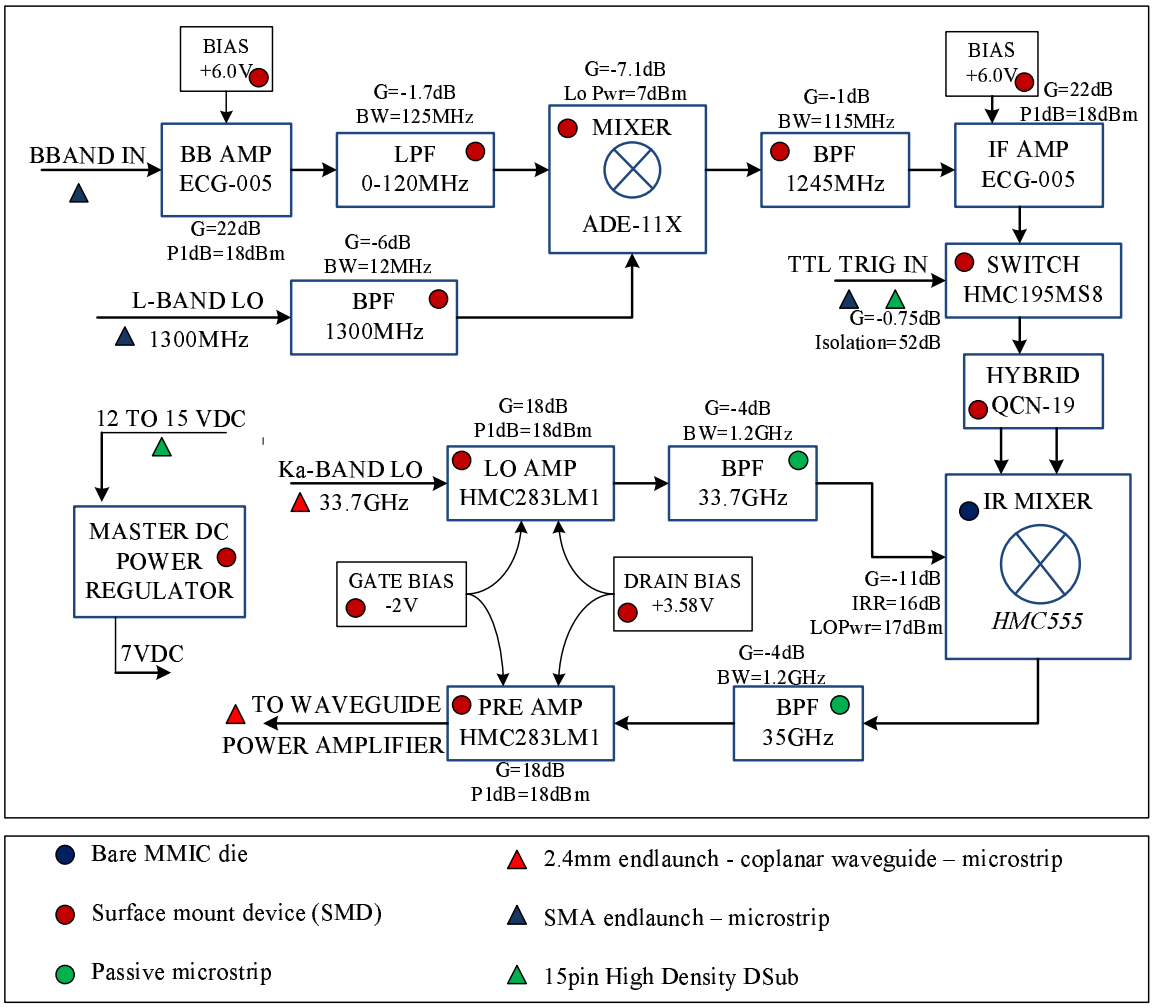

Figure 4.16. Block schematic of the Ka-band dual upconverter (transmitter).

figurations depending on the antenna requirements. A discussion on the choice of slot-configuration and the antenna design in terms of the analytical formulation and numeric simulation follows. A brief literature survey on slotted-waveguide antennas is also presented.

4.3.1 Slot configuration

Radiative slots on rectangular waveguides are conventionally cut in one of three configurations. They are (i) longitudinal slots on the broad wall offset from the center,

(ii) inclined slots on the broad wall, and (iii) inclined slots on the narrow wall. Figure 4.17 depicts these three configurations.

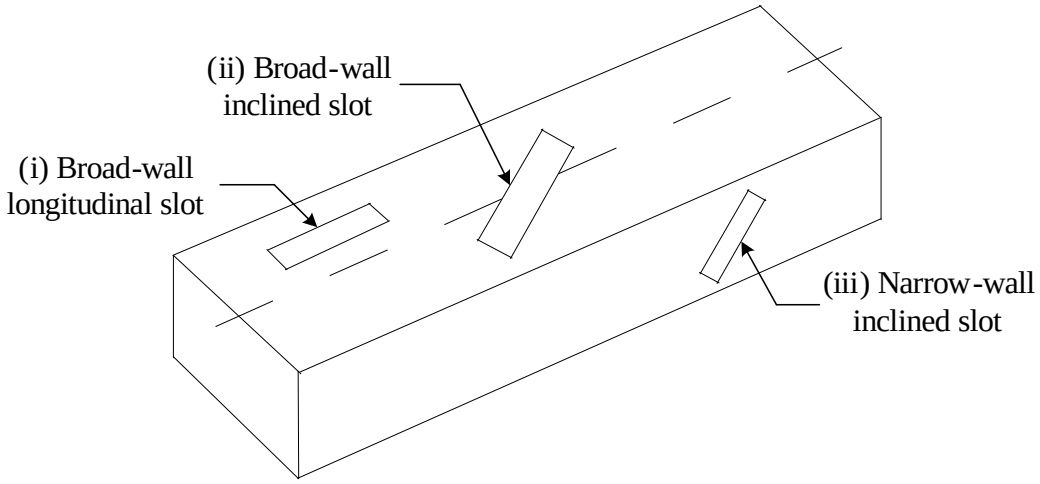

Figure 4.17. Commonly used configurations of radiative slots on a rectangular waveguide

Each of the above slots can be resonant or non-resonant. Non-resonant slot arrays are relatively complicated to design, and are usually used when a squinted beam is desired. Resonant slots are used for broadside beams, and are the preferred choice in this case.

Among the three slot configurations, the narrow wall inclined slots are not feasible in this case as their required inclination and length, makes them extend over to the broad wall, thereby preventing any kind of antenna arraying in the cross-track plane. The broad wall inclined slots are relatively simple to design, but lack polarization purity due to their orientation, and need polarization filters. Longitudinal shunt slots are easy to design, and have good polarization performance. However, their use as the interferometer antennas poses two problems.

Firstly, the required beamwidth of 45° in elevation requires some kind of arraying or beam restricting structure. The standard Ka-band waveguide dimensions (WR28) are such that placing two slotted-waveguides side-by-side to make an array would

introduce grating lobes in elevation. Secondly, the longitudinal slots are spaced half a guide wavelength apart and alternate on either side of the centerline such that the spacing introduces a phase shift of 180° between slots, and the alternate placement introduces an additional 180° of phase shift. This makes all the slots radiate in phase forming a broadside beam (see Figure 4.18). This alternating placement of the slots

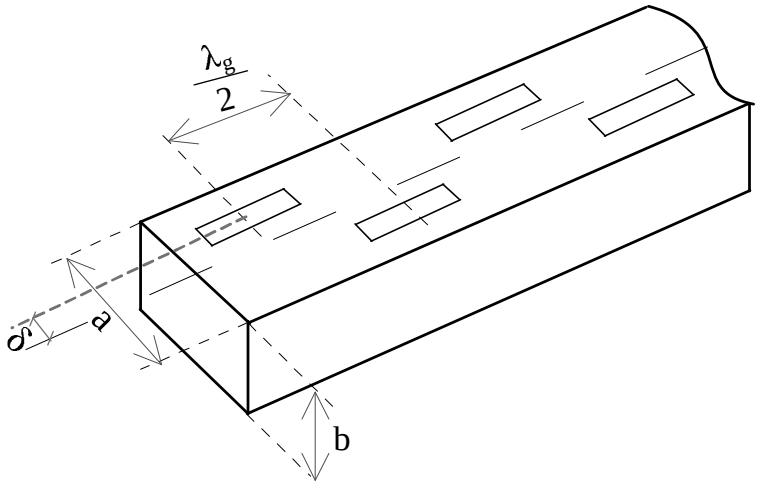

Figure 4.18. Sketch of a longitudinal shunt slotted-waveguide array

may result in grating lobes in planes other than the principal planes [4].

One solution to these two problems is to have the slots radiate into a parallel plate section that ends in a horn-like flare. Such a configuration is depicted in Figure 4.19. The parallel plates are spaced less than half a wavelength apart. Assuming that the antenna is very long, this spacing can only propagate the fundamental (parallel plate) TEM mode between them. The length and angle of the horn-like flare are adjusted to obtain the required elevation beamwidth and impedance match to free space.

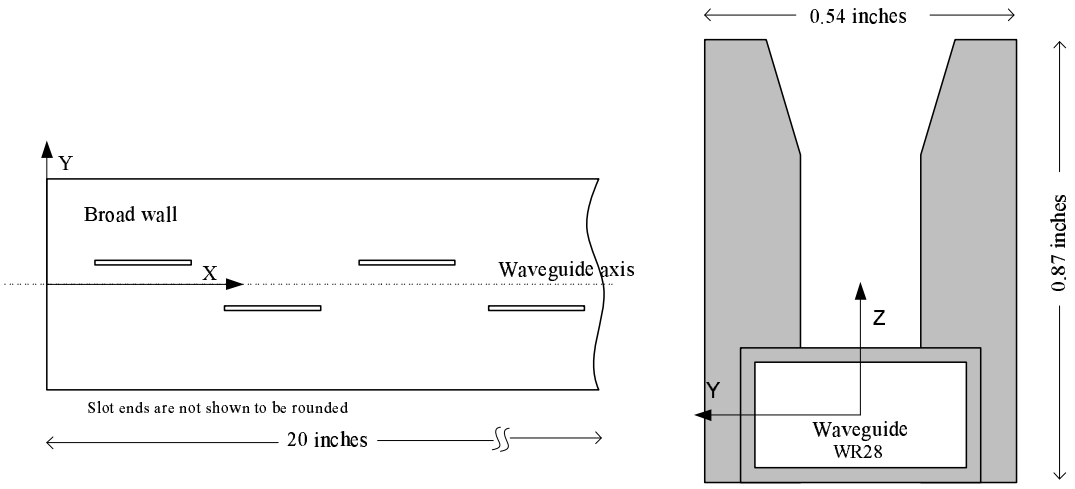

Figure 4.19. Sketch of the broad wall slots (left) and the antenna with the flares (right)

4.3.2 Analytical treatment

Although the final design of the antenna was refined using HFSS†, the initial design was based on analytical work from open literature. This was possible because slotted-waveguide antennas have been discussed in literature for several decades both analytically, computationally, and experimentally.

Although Watson [17] was the first to analyze slots in a rectangular waveguide, Stevenson [16] was the first to analytically deal with slots in rectangular waveguides as radiating elements. Stevenson showed that a longitudinal slot loaded the waveguide transmission line as a shunt element, and derived expressions for the resonant slot impedance assuming perfectly conducting, infinitesimally thin waveguide walls, and an infinite ground plane. Later Oliner [9] derived expressions for the shunt impedance of non-resonant slots, and accounted for the waveguide wall thickness as well. Apart from such analytical work, Stegen [15] made a repository of experimental data for longitudinal slot impedance.

---

†Short for High Frequency Simulation Software, a FEM based 3D full wave electromagnetic simulator from Ansoft Corp.

Much of the work mentioned above and more concerns slotted-waveguide antennas without the parallel plate and flange assembly. The theory in such literature nevertheless provides insight into the design process and working of the antenna. On the other hand, Gruenberg [4] derived an analytical expression for the impedance of a slot radiating into an infinitely long parallel plate section. Ramsay and Popovich [6] also discussed the use of such parallel plate sections to avoid off-principal plane grating lobes. However, to the best of the author's knowledge, a comprehensive analysis of slots radiating into parallel plate sections ending in a horn-like flare is not available in open literature.

The available analytical resources were used to arrive at a rough design which was refined using HFSS simulations. The antenna was designed with a transmission line matching viewpoint using expressions for the waveguide impedance, the slot impedance, and the impedance of the wave in the flared section which finally gets out as a free space wave with impedance of $\mathcal{Z}_{free} = 120\pi\Omega$. A discussion of this design process follows.

Gruenberg's [4] equation for impedance of a slot radiating into an infinitely long parallel plate section is

$$g = 2.75 \times 2.09 \times \frac{d\lambda_g}{\lambda^2}.\frac{a}{b}.\cos^2\left(\frac{\pi}{2}\frac{\lambda}{\lambda_g}\right)\sin^2\left(\frac{\pi\delta}{a}\right), \quad d < \frac{\lambda}{2}, \tag{4.1}$$

where g is the normalized (with respect to the guide conductance) slot conductance, a and b are the waveguide broad and narrow wall dimensions, λ_g is the guide wavelength, and δ is the slot offset from the center of the broad wall (see Figure 4.18). Figure 4.20 shows a plot of slot conductance given by (4.1) for different slot offsets from the center of a WR28 waveguide when the parallel plates are separated by $d = 0.4\lambda$. The slots being placed $\lambda_g/2$ apart, appear to the transmission line as though they were in parallel at the same location. If each one of them has a normalized conductance g (no amplitude weighting in the H-plane), then an array of n such slots will be matched

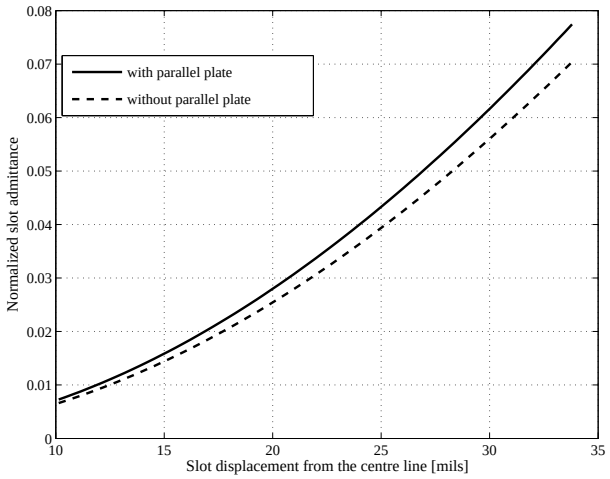

Figure 4.20. Normalized conductance of a longitudinal slot on the broad wall of a rectangular waveguide

to the transmission line if $ng = 1$, and if the array is terminated in an open circuit (zero conductance). An open circuit is easily obtained by a short circuit and a $\lambda_g/4$ transformer. This configuration is depicted in Figure 4.21.

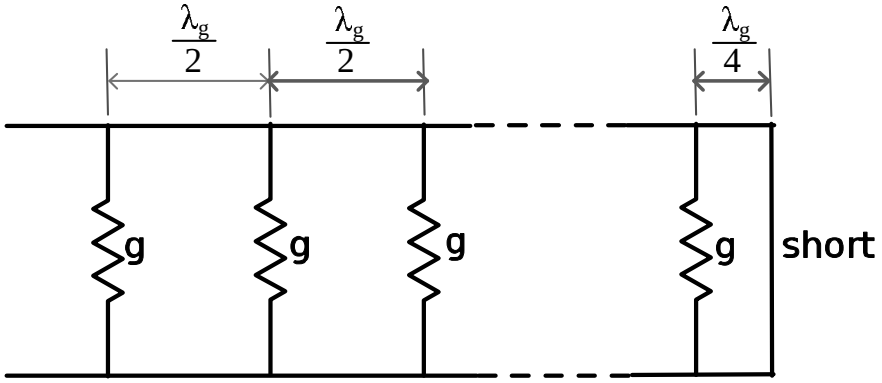

Figure 4.21. Circuit equivalent of the slotted-waveguide antenna array

The other part of the matching problem is to match the wave radiated by the slots to free space through the parallel plate and flares. The wave in the flared section (see Figure 4.23) is similar to the TE_0 mode in a wedge waveguide [13], and its wave-impedance is given by,

$$\mathcal{Z}_{flare} = \frac{2\pi j f \mu}{k} \frac{H_0'^{(1)}(k\rho)}{H_0^{(1)}(k\rho)}. \tag{4.2}$$

Here, ρ is the radial length along the wedge, $H_n^{(1)}$ is the Hankel function of the first kind or order n, and μ is the permeability of the space within the wedge plates. Figure 4.22 shows the impedance matching between the wedge mode and free space for different ρ.

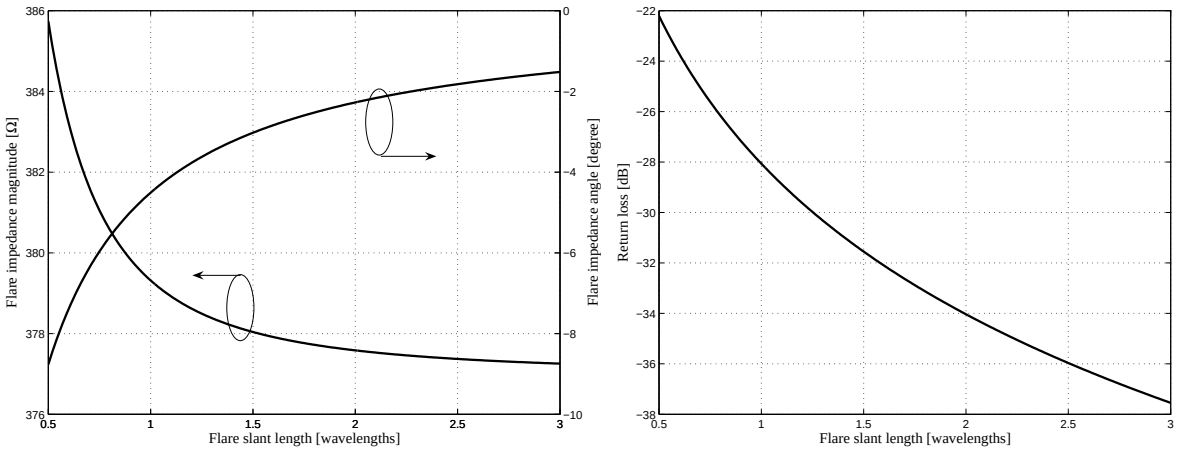

Figure 4.22. Wave impedance for the fundamental TE_0 mode in a wedge waveguide

Impedance matching can be achieved by a smooth transition from the parallel plate mode to the wedge mode, and by matching the wave impedance at the open end of the wedge to that of free space. This condition when imposed on (4.2) requires ρ to be greater than a wavelength for a theoretical return better than 30dB. The length of the parallel plate section itself is chosen such that it considerably attenuates modes other than the fundamental TEM mode while providing a smooth transition into the flared section. This length is typically chosen to be about one wavelength long [6].

For the chosen value of ρ, the flare angle α should be adjusted to get the desired E-plane radiation pattern. The radiation pattern in the E-plane due to a E-plane flare is an analytically well known problem. Equivalence between the elevation patterns (E-plane pattern) of the flare and a TE_{10} rectangular waveguide E-plane horn can be

drawn, because both have identical field distributions and geometries in the E-plane. This geometry and field distribution are depicted in Figure 4.23.

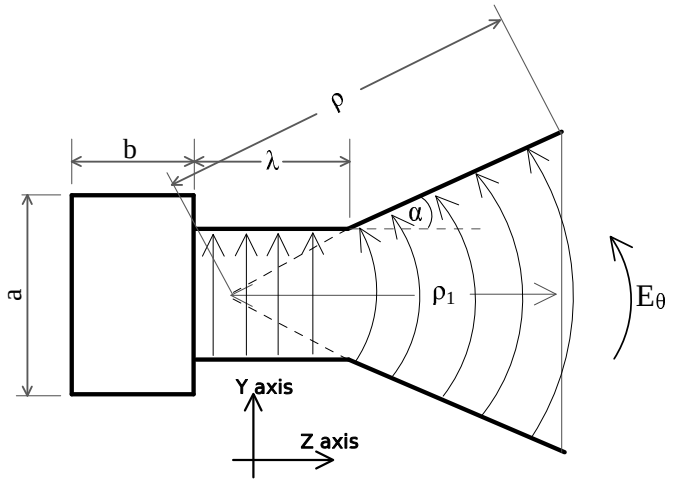

Figure 4.23. Geometry and electric field in the E-plane of an E-plane horn and the flared slotted-waveguide antenna

The E-plane electric field is given by $E_r = E_\phi = 0$ and,

$$E_\theta = -j\frac{a\sqrt{\pi k\rho_1}E_1 e^{-jkr}}{8r}\left(-e^{j(k\rho_1\sin^2(\theta/2))}\left(\frac{2}{\pi}\right)^2(1+\cos\theta)\mathcal{F}(t_1',t_2')\right), \qquad (4.3)$$

where E_1 is the magnitude of the y-directed electric field at the beginning of the flare, ρ_1 is the flare length (see Figure 4.23), t_1' and t_2' are given by

$$t_1' = \sqrt{\frac{k}{\pi\rho_1}}\left(-\frac{b_1}{2} - \rho_1\sin\theta\right),$$

$$t_2' = \sqrt{\frac{k}{\pi\rho_1}}\left(+\frac{b_1}{2} - \rho_1\sin\theta\right),$$

and $\mathcal{F}$ is related to the Fresnel integrals[†] as

$$\mathcal{F}(t_1,t_2) = [\mathcal{C}(t_2) - \mathcal{C}(t_1)] - j[\mathcal{S}(t_2) - \mathcal{S}(t_1)].$$

[†] $\mathcal{C}(x) = \int_0^x \cos\left(\frac{\pi}{2}t^2\right)\,dt$ and $\mathcal{S}(x) = \int_0^x \sin\left(\frac{\pi}{2}t^2\right)\,dt$

To arrive at a beamwidth of 45° based on these equations the flare angle α was chosen to be 22°. The resulting E-plane pattern is shown in Figure 4.26.

To simulate the antenna array within the finite computational resources of the computer, a HFSS model for a unit cell was built containing two slots on either side of the center-line, and the periodic (or master-slave) boundary condition was used. The HFSS geometry and its equivalent circuit are shown in Figure 4.24. Such a boundary condition is equivalent to solving for the impedance of the slots (which are dependent on the mutual coupling between the slots) placed in an infinite array. Since the mutual coupling between slots is negligible beyond the first two to three neighbors (on either side) this boundary condition gives a good estimate of slot impedances for all slots but for a few slots on either end of the antenna. This is not of concern in this case as the antenna being long (about 90 slots), the contribution from a single slot to the overall impedance is small.

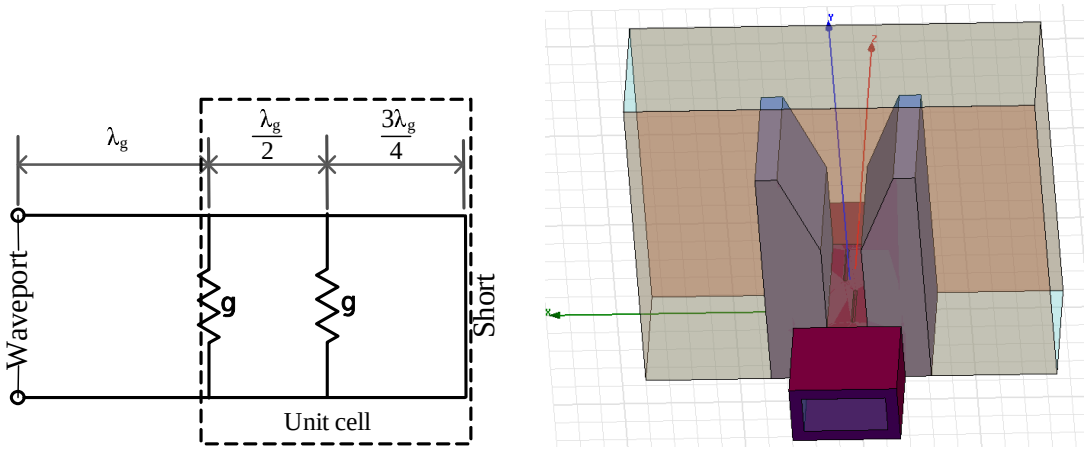

Figure 4.24. HFSS geometry (right) and its circuit equivalent (left) of a unit cell used to simulate slot impedance in a long array

HFSS simulations were carried out to design for slot length, width, and separation keeping in mind physical, and machining constraints. The normalized slot impedance was computed using the one-port $\mathcal{S}$ parameter or reflection coefficient, Γ_{cell} as

$$g = \frac{1 + \Gamma_{cell}}{1 - \Gamma_{cell}}. \tag{4.4}$$

The normalized impedance of n such slots forming $\frac{n}{2}$ units cells is $\frac{ng}{2}$, giving an antenna input return loss of

$$\Gamma_{ant} = \frac{ng - 2}{ng + 2}. \tag{4.5}$$

The final design has 89 slots and each slot is 12 mils wide and 162.54 mils long, has completely rounded ends, and is displaced 18.15 mils off the center. The slot location and dimensions are depicted in Figure 4.25.

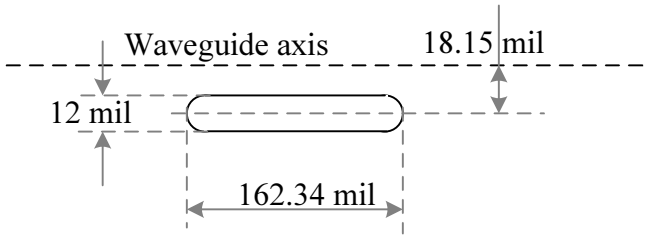

Figure 4.25. Location and dimensions of the slots in the final antenna design

Figure 4.26 shows the simulated antenna E-plane pattern for the final antenna design. The theoretical and simulated E-plane patterns agree with each other. It is shown in Chapter 5 that the measured E-plane pattern agrees well with the theoretical pattern (see Figure 5.24). The H-plane pattern on the other hand, is primarily dictated by the array factor, making the theoretical and simulated patterns the same. The theoretical H-plane pattern is plotted in Chapter 5 (see Figure 5.24).

Figure 4.27 shows pictures of the manufactured antenna[†]. Figures 5.23 and 6.1 from Chapter 6 also show these antennas.

[†]Precision metal milling operation for the flanges and slots was done at Amherst Machines Co., Amherst MA.

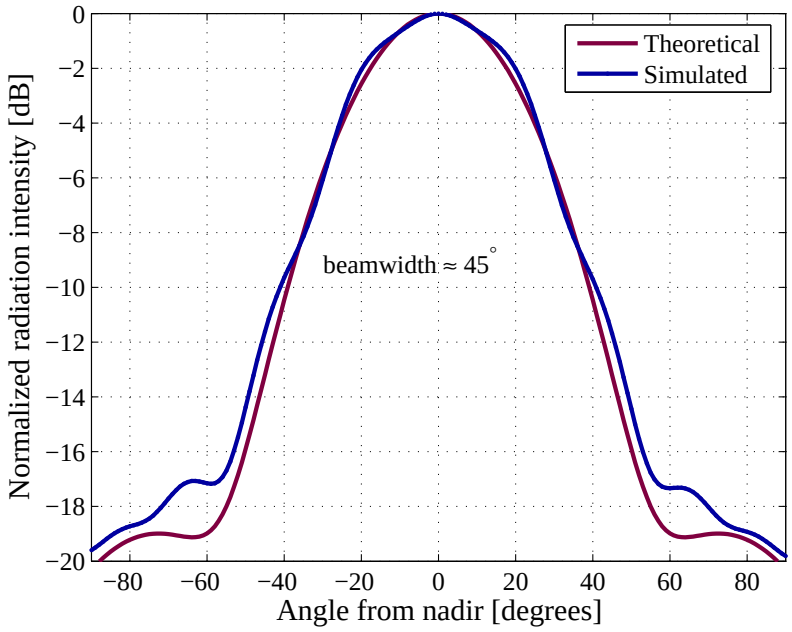

Figure 4.26. Simulated and theoretical E-plane pattern of the interferometer antennas

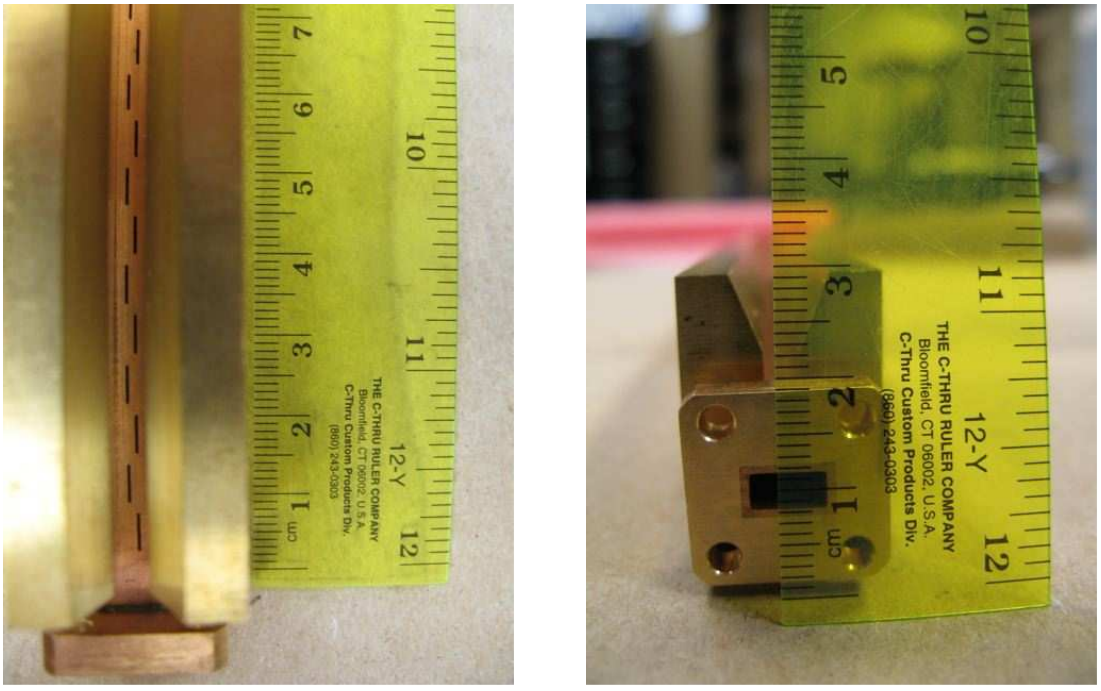

Figure 4.27. Pictures of the manufactured slotted waveguide antenna

CHAPTER 5

RADAR HARDWARE EVALUALATION

After design and fabrication, the radar receiver, transmitter, and antennas were evaluated in the laboratory and their performance was compared with the design specifications. This chapter discusses the results from the laboratory evaluation of the radar hardware.

5.1 Dual-Downconverter

The Dual-Downconverter (DDC) is the most performance critical part of the radar hardware, and its evaluation covers the bulk of this chapter. The DDC was mainly evaluated for bandpass characteristics such as return-loss, noise-figure, image-rejection, non-linearity, gain-flatness, and thermal characteristics such as phase and amplitude stability over temperature. The experimental setup and results of the bandpass characterization are presented below.

5.1.1 Bandpass characteristics

5.1.1.1 Return Loss

The Return loss on the two Ka-band input channels is required to be better than 7dB. The RF signal is fed into the downconverter using an end-launch assembly from Southwest microwave (see Figure 5.1). Since the connector is mechanically affixed to the PCB, the contact between the connector pin and the PCB trace wiggles due to external torques on the connector from housing walls and co-axial cables. This wiggle changes the matching properties considerably. The reflection coefficient at

the two RF channels was measured after extensive wear and tear (several months) of the connector contact without repositioning it on the trace. Figure 5.1 shows the input matching on the two RF channels measured using the HP8722C Vector Network Analyzer[†]. It was also observed that the reflection coefficient improved by 2-3dB when the connector pin was centered on the trace after extensive use.

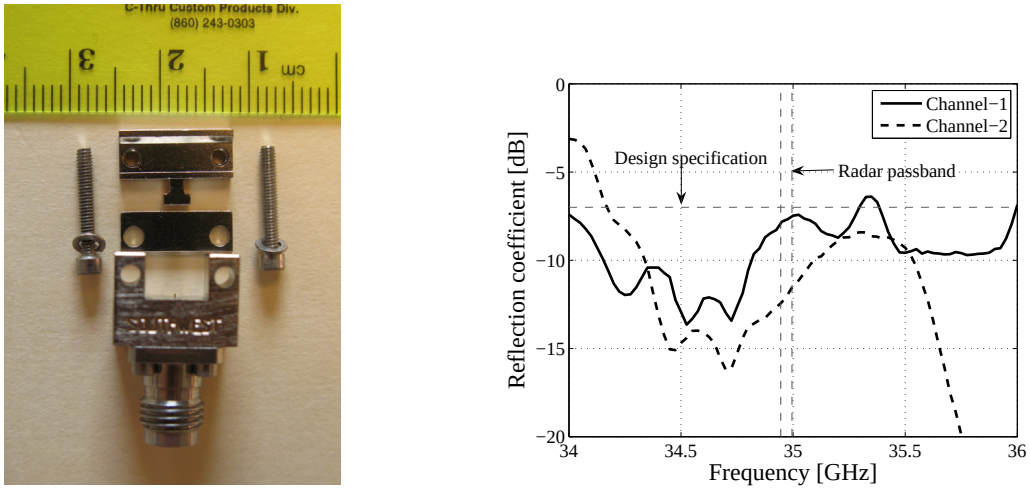

Figure 5.1. Picture of the 2.4mm end-launch connector (left) and a plot of the reflection coefficient at their input (right)

5.1.1.2 Noise figure

The noise figure of the downconverter was estimated by measuring the system gain, G, and the output noise power, N_{out} with a known noise source at the input, N_{in}. Bandpass gain was measured by successively injecting monotones spanning the radar bandwidth with known power levels, P_{in}, into the RF input of the radar and measuring the baseband output power, P_{out} on a spectrum analyzer[‡]. At every frequency point, the noise figure is given by,

[†]Now obsolete

[‡]The spectrum analyzer used for measurement throughout this work is the Advantest U3772.

$$NF = \frac{N_{out}}{N_{in}} \frac{P_{in}}{P_{out}}. \tag{5.1}$$

A known N_{in} can be obtained by terminating the RF input with a 50Ω resistance at room temperature, $T = 300$K, giving

$$N_{in} = kTB = -174dBm + 10\log_{10} B \;\; [dBm].$$

Here, B is the equivalent noise bandwidth that is related to the resolution bandwidth of the spectrum analyzer, and k is the Boltzmann's constant. This method of measuring noise figure is called the direct method and is not an accurate method. The more accurate Y-factor method could not be employed due to the non-availability of a calibrated cold and hot noise source at Ka-band. The uncertainities in the direct method measurement is mainly due to (i) error in the power meter measurement of P_{in}, (ii) error in the estimate of resolution bandwidth of the spectrum analyzer, and (iii) error in the measurement of P_{out} relative to N_{out}. These errors can be quantified as follows.

From the instrument specifications, it is known that the power meter[†] measurement accuracy, zero error, and non-linearity contribute to less than ±0.05dB of error. Error in the measurement of N_{out} relative to P_{out} is given by the scale-fidelity of the spectrum analyzer used for the measurements, which is specified to be within ±0.5dB. The error in equivalent bandwidth on the other hand is difficult to estimate. The filter determining this equivalent noise bandwidth (usually a 4-pole synchronously tuned filter) does not have a maximally flat response in order to maintain good time domain response. Based on the response of such filters, assuming the equivalent noise bandwidth to be the resolution bandwidth would under determined it by a factor of

[†]The Agilent 8487D power sensor with the Agilent N1911A P-series power meter

0.52dB[†]. This value was added to the N_{out} measurements. The measured noise figure after the bandwidth correction along with error bars (due to power meter error and scale-fidelity) is shown in Figure 5.2[‡]. The increase in noise figures of about 3dB at the higher end of the radar bandwidth if due to thermal noise from one of the image bands. This is discussed along with the image rejection measurements.

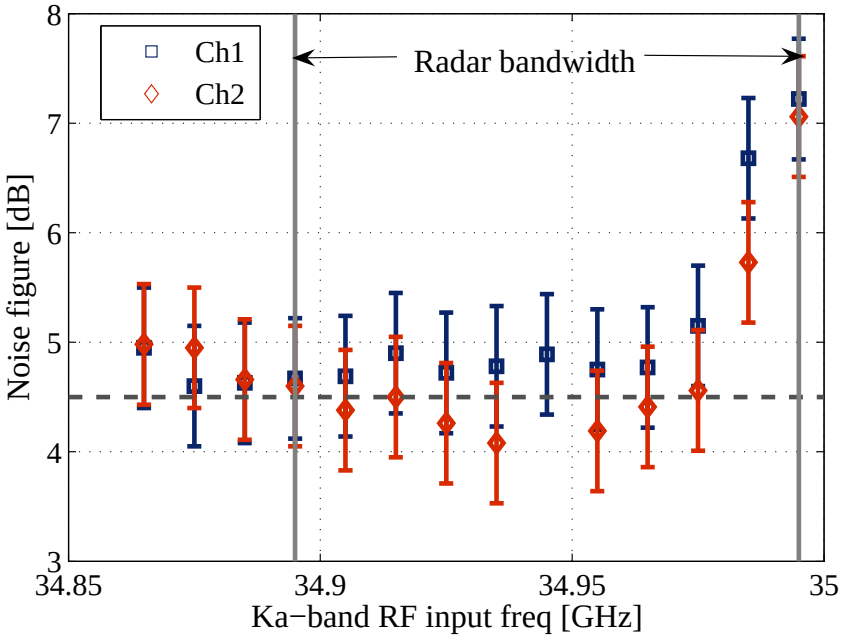

Figure 5.2. Measured noise figure of the Ka-band dual-downconverter

5.1.1.3 Image rejection

As mentioned earlier, image-rejection at the Ka-band to L-band downconversion is obtained partly by a filter and mostly by an image-reject mixer. Image rejection at the L-band to baseband downconversion is obtained using an image-reject filter (see Figure 4.9). Due to the two stages of downconversion, there are four possible Ka-band RF bands that can downconvert to the same baseband of 5 MHz to 105 MHz. These

[†]See http://cp.literature.agilent.com/litweb/pdf/5966-4008E.pdf or [5]

[‡]One of the points on Channel 2 is missing owing to it being classified as an outlier.

four RF bands are shown in Figure 5.3. In this figure,"RF band" is the desired band carrying the radar signals. "Image 1" is the image of the RF band at the first downconversion stage that is rejected by the RF filter and the image-reject mixer. "Image 2" is the band that is not rejected at the first downconversion stage and appears as an image at the second downconversion stage. This band is rejected (somewhat) by the image-reject filter before the second downconversion mixer. "Image 3" is the band that is an image at both stages of downconversion that is well rejected and is of little concern. Image 1 and Image 2 on the other hand can be of concern in terms of out of band noise and interference. Figure 5.4 shows the Image Rejection Ratio (IRR) for these two image bands and a close up of the image-rejection for Image 1 band. It can be seen that Image 1 meets the specification of 30dB. Image 2 however is not well rejected due to the large bandwidth and close proximity of the L-band RF band to the L-band LO. It must be noted that this low image-rejection results in an increase in noise figure at the low frequency end of the baseband as can be seen in Figure 5.2.

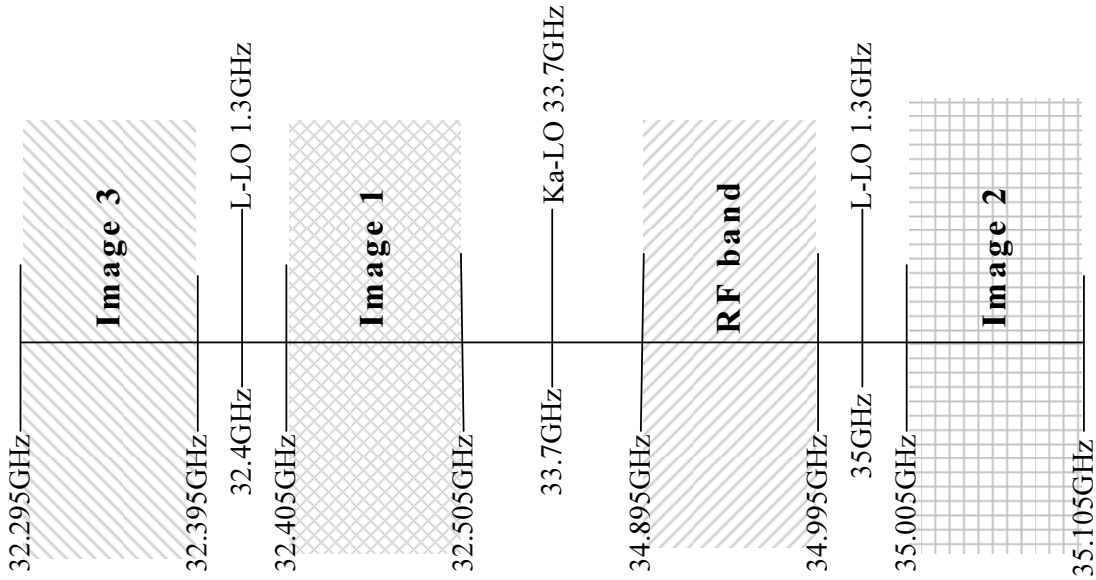

Figure 5.3. Different image bands in the Ka-band dual downconverter

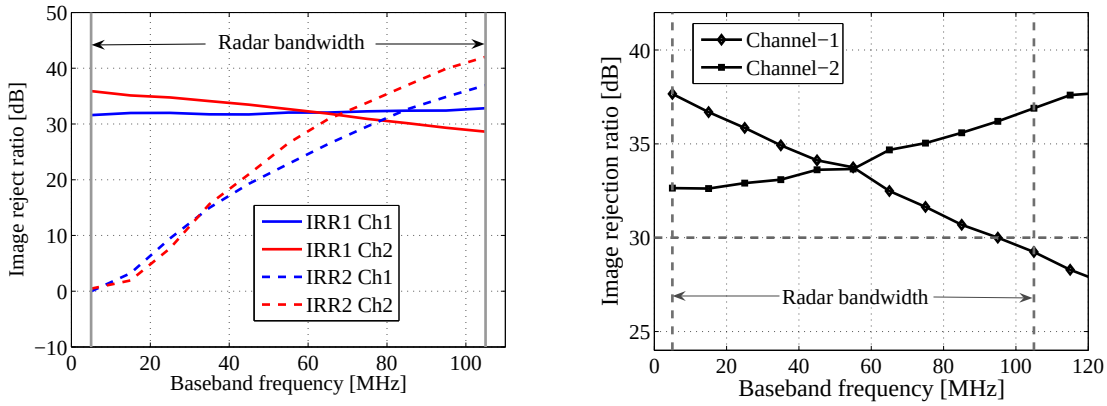

Figure 5.4. Image rejection ratios of the Ka-band dual downconverter

5.1.1.4 Output non-linearity

Radars receive signals over a wide dynamic range owing to the wide differences in range to target, and due to desired or undesired transmitter leakage and external interference. Most radar science theories used in processing data assume linearity of downconversion hardware. Linearity here is a misnomer due to the existence of mixing devices. In this context, linearity implies linearity in the baseband signal as a function of the radar received RF signal notwithstanding the frequency translation. This linearity can be characterized by the power in various harmonics and intermodulation products relative to the power in the desired fundamental. Figure 5.5 shows a plot of the dual downconverter output power (at baseband) versus input power (at Ka-band). It can be seen that for low input powers (less than 65dBm) the downconverter is fairly linear, in that, increments in the input power (in dBm) give the same increments in the output power. It can be seen from Figure 5.5 that the specified Ka-band input power range from -100dBm to -65dBm in Table 4.1 falls within the linear range of the downconverter. However, depending on the isolation between the antennas, the leakage of transmitted power into the receiver may not fall into the linear range. This must be taken into consideration if pulse to pulse calibration (of phase or power) using this transmitter leakage signal is desired. A metric for the amount of non-

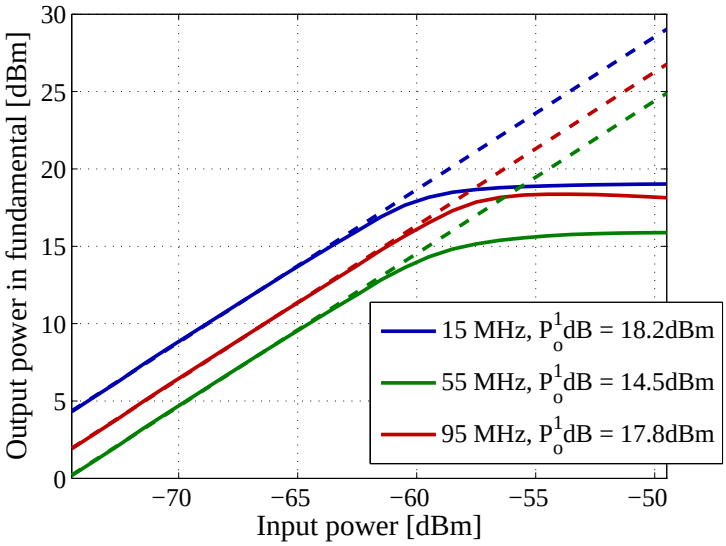

Figure 5.5. Output 1dB compression point, P^1_odB of the Ka-band dual downconverter.

linearity in the downconverter is the ratio of power in the second harmonic to that in the fundamental and the ratio of the power in the third harmonic to that in the fundamental and so on. Figure 5.6 shows these ratios as a function of input RF power.

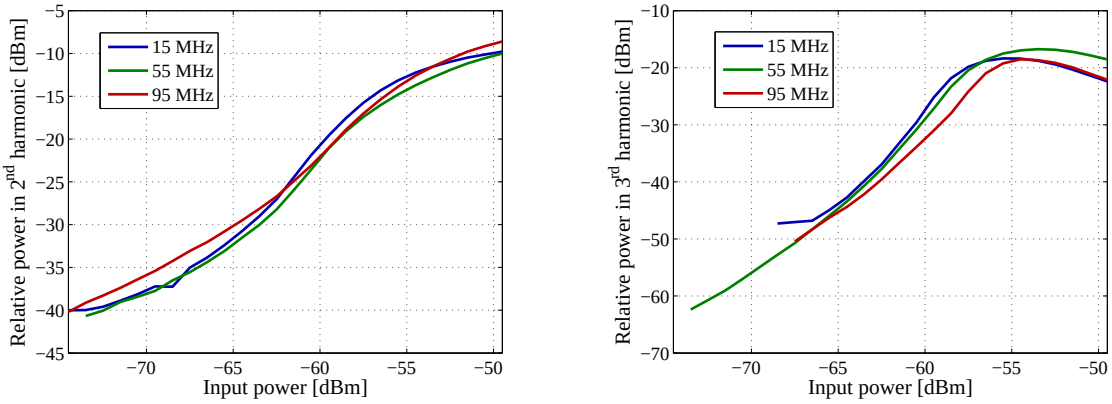

Figure 5.6. Power level of second (left) and third (right) harmonics relative to the fundamental at the output of the Ka-band dual downconverter

5.1.1.5 Gain flatness

The actual gain of the dual downconverter depends on the LO power levels and temperature of the various active components. Gain variation and inter-channel gain difference over the radar bandwidth and temperature are much more of a concern than the absolute gain of the channels themselves. With this in mind, gain measurements were made by injecting different monotones spanning the radar bandwidth at a known power level, P_{in}, and by measuring the baseband power, P_{out} over different ambient temperatures. Since absolute gain was not of particular interest, P_{in} was assumed to be the power output setting on the signal generator[†] less the insertion loss of the cable feeding the RF input to the downconverter, and P_{out} was assumed to be the power computed from the RMS voltage of the baseband signal read out by a digital oscilloscope[‡]. In other words, no corrections or error bars on either P_{in} or P_{out} were applied. Figure 5.7 shows a plot of the downconverter gain versus baseband frequency for the two channels at different temperatures. The figure shows a gain variation over the radar bandwidth of about 4.5dB on one channel and about 2dB on the other. The rather ambitious specification of 2dB gain variation over a 5 MHz to 105 MHz bandwidth was achieved for only one channel. Moreover, Figure 5.7 shows that a variation exceeding 1.5dB is possible due to changing temperature alone. This requires a temperature-gain calibration to meet the specifications. Such a calibration table was constructed by measuring the downconverter gain for various frequencies and temperatures. This table is depicted as an image in the frequency-temperature dimensions in Figure 5.8 A more important gain parameter is the dB-difference between the gains of the two channels. This difference computed from the gain values in Figure 5.8 is shown as an image in the frequency-temperature

[†]The Agilent E8257D

[‡]The oscilloscope used throughout this work was the Agilent MSO6104A.

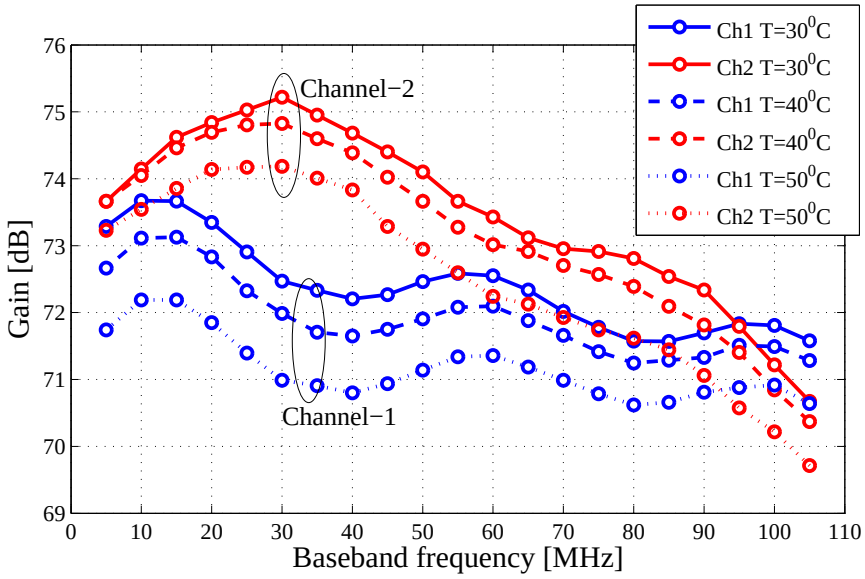

Figure 5.7. Ka-band dual downconverter gain versus baseband frequency at different temperatures

dimension in Figure 5.9. The values in these images were repeatable to better than 0.5dB, ensuring good gain-temperature calibration.

5.1.2 Phase stability

Phase stability is more difficult to estimate and characterize compared to the previously documented bandpass characteristics. It is desirable that the phase changes at the downconverter output occur only due to phase changes in the two channel input signals themselves. However, there exist other factors affecting the inter-channel phase, both deterministic and random that have to be accounted for in the error budget. Primary among these factors are (i) change in RF line lengths due to thermal expansion, (ii) change in dielectric constant with temperature, especially at the Teflon knee (described later), (iii) change in insertion phase of the active components with temperature and bias conditions, (iii) thermal noise, and (v) variance of the estimator itself. Each of these factors is discussed briefly below.

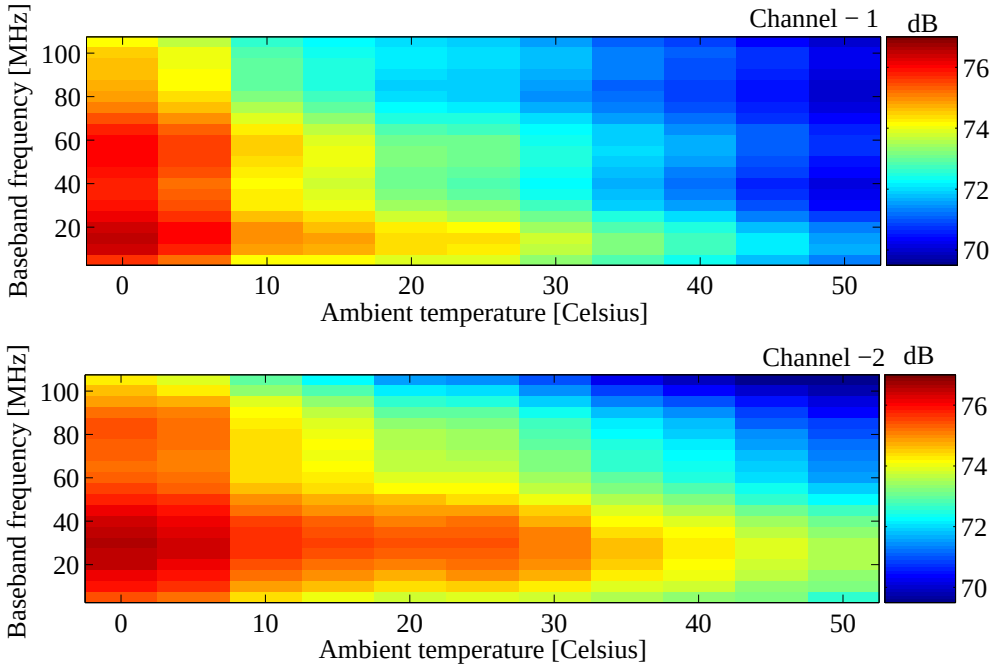

Figure 5.8. Ka-band dual downconverter gain as a function of baseband frequency and temperature

5.1.2.1 Factors affecting phase noise

(i) Change in physical temperature results in expansion and contraction of metal lines like microstrip traces and co-axial cables, and changes their insertion phase. Temperature gradients across the two downconversion channels can result in a thermal expansion driven component of inter-channel phase. For instance, Copper lines having a coefficient of thermal expansion (linear) of $17 \times 10^{-6}/°\text{C}$ at 35GHz would result in an insertion phase change of 8.7 mdeg per degree centigrade per every wavelength of line. Using these numbers, a differential temperature of just 0.1°C across the front end RF cables of the two channels one foot in length can result in a thermal expansion driven inter-channel phase component of about 40 mdeg, easily detectable by the measurement system employed to characterize the downconverter.

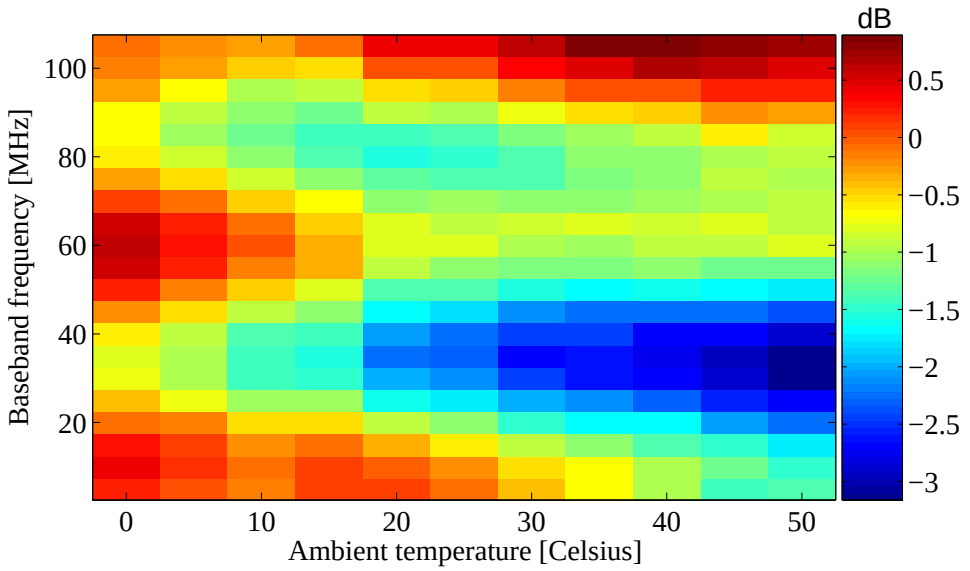

Figure 5.9. Difference in dB gain between the two Ka-band dual downconverter channels as a function of baseband frequency and ambient temperature

(ii) The term teflon knee[†] refers to a change in the microscopic structure of Teflon. Commercial co-axial cables use a type of Teflon called poly-tetrafluoro-ethylene or PTFE as the dielectric. The insertion phase of such cables are affected by two processes. They are (a) thermal expansion of the center conductor as discussed previously, and (b) change in dielectric constant of PTFE with temperature. PTFE undergoes structural changes at the microscopic level near some temperatures. The most drastic among them in terms of insertion phase occurs at about 19°. This is referred to as the Teflon Knee. Figure 5.10 shows the insertion phase in parts per million (PPM) versus temperature for some of the cables manufactured by Micro-coax as an example. As an estimate of the magnitude of insertion phase change that can result by crossing the Telfon knee, the same foot long co-axial cable was considered. A relative change in insertion phase of the order of 500PPM (see Figure 5.10) in the cable at 35GHz implies a change in insertion phase of a foot long cable of about 6

[†]A brief account of the Teflon knee and its effect on the insertion phase of a typical co-axial cable maybe found at http://www.micro-coax.com/pages/technicalinfo/applications/27.asp or in [5].

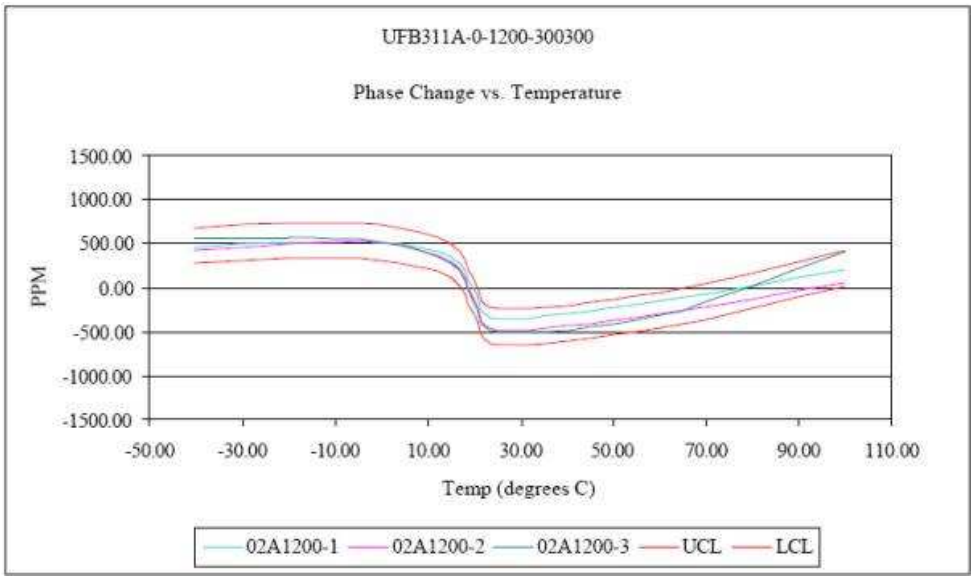

Figure 5.10. Insertion phase of a typical PTFE cable

degrees. Assuming the trend to be linear on the knee, a temperature gradient of even 0.1° across channels can result in a Teflon-knee driven inter-channel phase component of 60 mdeg on the knee. The actual effect on inter-channel phase depends on the actual cables used and their lengths. These numbers however suggest that this effect can be significant. A possible solution to this would be to use special phase stable cables having Silicon di-oxide (SiO_2) as the dielectric. These cables are however much more expensive and are not easily available. SiO_2 cables were never used in the experiments described henceforth due to prohibitive lead-times in their procurement.

(iii) Active components may have phase responses that vary with temperature and bias conditions. Most manufacturers do not publish such characteristics in their data sheets, and their contribution to inter-channel phase is difficult to estimate and characterize. For the remainder of this work, it has been assumed that such contributions are negligible, especially because identical active component catalog items make up the two downconversion channels.

(iv) Thermal noise can change both amplitude and phase of a signal, and has both in-phase (real) and quadrature-phase (imaginary) components in the complex phasor

domain. Figure 5.11 depicts the effect of thermal noise on the phase of a monotonic sinusoid. Additive white thermal noise can be visualized as a ball around the signal vector. The resultant of the signal and one realization of the noise vector is shown in the figure. The RMS phase error due to such an additive thermal noise can be shown to be

$$\sigma_\phi = \frac{1}{\sqrt{2SNR}}. \tag{5.2}$$

As an example, for a noise-bandwidth of 100 MHz, noise figure of 5dB, input RF

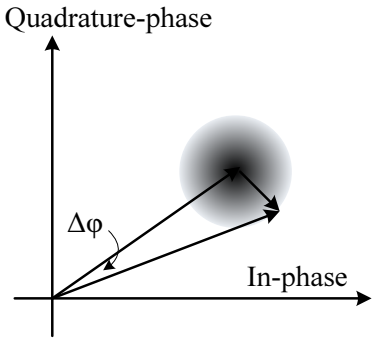

Figure 5.11. Sketch depicting the effect of thermal noise on the phase of a monotone

signal of -100dBm, and a gain of 74dB will result in an output SNR of about 10dB that gives a phase standard deviation of 200 mdeg. In reality, single point phase estimates are seldom made, and the SNR in (5.2) multiplies by an integration improvement factor that depends on the number of points used for phase estimation and their coherence.

(v) The estimator variance accounts for the variance in the phase estimates given by the phase estimation algorithm and is discussed later.

All the above factors contribute to the phase stability of the downconverter in terms of stability of the two channels themselves and stability in the phase difference between them. The experimental setup and estimation algorithms used for characterizing this phase stability are taken from a previous Master's thesis work of Amhed

[12]. A brief description of the experimental setup and the phase estimation algorithm follows.

5.1.2.2 Experimental setup

Figure 5.12 shows the block diagram of the experimental setup used for phase estimation. The dual downconverter along with a rat-race power divider was placed

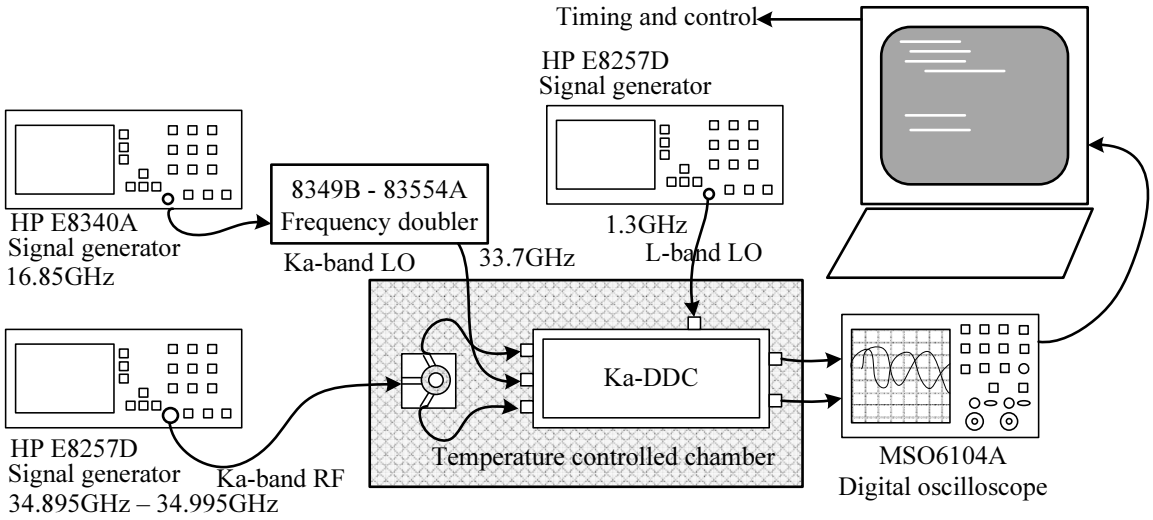

Figure 5.12. Block schematic of the experimental setup used in phase stability measurements

inside a thermally controlled environment. The different thermal environments used were (i) ambient air-conditioning and temperature control in the lab premises, (ii) thermally insulated environment of a portable ice chest, and (iii) the EC12[†], a liquid carbon di-oxide (LCO2) cooled environmental chamber. The two local oscillators are obtained from signal generators. The Ka-band LO in particular, had to be generated at a sub-harmonic and passed through a microwave power amplifier and frequency doubler due to the non-availability of Ka-band signal generators. The input Ka-band RF signal is a monotone generated by another signal generator, and is split into the two channels by a rat-race hybrid. The two output baseband channels are sampled

[†]Manufactured by Sun Electronic Systems. See [5] for instrument catalog and datasheet.

by a digital oscilloscope, and the digital data thus recorded is sent to a host controller computer via an ethernet link. This computer runs a MatLab script that estimates the phase of the two channels. The computer also controls the temperature chamber and the signal generators, and reads out telemetry information (temperature) from the on-board temperature sensors on the downconverters. The phase and temperature data are stored to disk and also displayed in real time. The heart of this phase measurement process is the phase estimation algorithm used by the MatLab script. A brief description of this algorithm follows[†].

5.1.2.3 Phase estimation algorithm

Modelling the effect of noise of different kinds on the amplitude and phase of a signal is a mathematically involved proposition. Significant simplifications can be made in the analytical formulation if the changes in amplitude and phase can be modeled as an additive noise. This assumption is fairly accurate if the signal to noise ratio is large. With this assumption, a vector of N observed time samples of a monotone given by $\mathbf{S} = [s_1\ s_2\ s_3\ \ldots\ s_N]^T$ can be represented as an addition of a "model" and a noise vector $\mathbf{V} = [v_1\ v_2\ v_3\ \ldots\ v_N]^T$. The model fitted to the data consists of the parameters that define the data- the amplitude, A, and phase, ϕ in the case of a monotone, and an operator, H, projecting these parameters into a time series. This can me mathematically represented as,

$$\mathbf{S} = H\mathbf{\Theta} + \mathbf{V} \tag{5.3}$$

where $\mathbf{\Theta}$ belongs to the parameter space, which in the case of a monotone is $\mathbf{\Theta} = [A\ \ \phi]^T$. Many algorithms exist which fit a suitable model according to (5.3). The most common among them is the Maximum Likelihood Estimation or MLE. MLE

[†]A detailed account of the algorithm and its properties are documented in [12] and [11].

estimates the value of $\mathbf{\Theta}$ as the one that most probably gave rise to the observation S. In other words, given an observation S, the best parameter fit is the one that maximizes the probability of that observation occurring. Mathematically this is represented as

$$\hat{\mathbf{\Theta}} = \max_{\mathbf{\Theta}}[\mathcal{P}(\mathbf{S} \mid \mathbf{\Theta})], \tag{5.4}$$

where $\hat{\mathbf{\Theta}}$ is the MLE estimate of the parameter space. The conditional probability in (5.4) can be evaluated if the statistical properties of the noise vector $\mathbf{V}$ are known. Assuming the noise vector to be a Gaussian random vector with correlation matrix R, the conditional probability in (5.4) can be written as

$$\mathcal{P}(\mathbf{S} \mid \Theta) = \frac{1}{\sqrt{(2\pi)^N \mid R \mid}} \exp\left[-\frac{1}{2}\mathbf{V}^T R^{-1}\mathbf{V}\right]. \tag{5.5}$$

This probability can be maximized by maximizing the argument of the exponential. It can be shown that this exponent achieves its maximum value when

$$\hat{\mathbf{\Theta}} = \left(H^T R^{-1} H\right)^{-1} H^T R^{-1}\mathbf{S}. \tag{5.6}$$

To solve the above equation for $\hat{\mathbf{\Theta}}$, R and H have to be known. Assuming the noise samples to be identically distributed, uncorrelated Gaussian random variables with variance σ^2, the covariance matrix R can be written as $R = \sigma^2 I$, where I is an $N \times N$ identity matrix. The easiest way to deal with the operator H is by linearizing it using a Taylor expansion around an initial estimate of the parameter vector $\mathbf{\Theta_0}$ as

$$\mathbf{S}(\mathbf{\Theta}) = \mathbf{S}(\mathbf{\Theta_0}) + \frac{\partial \mathbf{S}(\mathbf{\Theta_0})}{\partial \mathbf{\Theta}}\left(\mathbf{\Theta} - \mathbf{\Theta_0}\right), \tag{5.7}$$

which in the case of a monotonic cosinusoid with frequency f and unit amplitude becomes

$$\cos(2\pi f t + \phi) = \cos(2\pi f t + \phi_0) - \sin(2\pi f t + \phi_0)(\phi - \phi_0). \tag{5.8}$$

Using this, (5.6) becomes

$$\hat{\mathbf{\Theta}} = \left(\mathbf{H}_1^T R^{-1} \mathbf{H}_1\right)^{-1} \mathbf{H}_1^T R^{-1} \left(\mathbf{S} - \mathbf{H}_0\right), \tag{5.9}$$

where

$$\mathbf{H}_1 = -\sin(2\pi f t + \phi_0),$$

and

$$\mathbf{H}_0 = \cos(2\pi f t + \phi_0) + \sin(2\pi f t + \phi_0)\phi_0.$$

Hence, given an initial phase ϕ_0, a phase estimate can be computed. This value can be used as ϕ_0 and the whole process repeated giving an iterative algorithm.

A detailed account of the estimator performance may be found in [12]. However, it is important to mention here two of its properties without proof. Firstly, the iterative algorithm mentioned above for phase estimation always converges to the true phase contingent to the assumptions about noise being true. Secondly, the estimator is unbiased and efficient. Bias and efficiency in an estimator are related to accuracy and precision respectively. The LSE estimator described above is unbiased or accurate in that, the expected value of the phase estimated by the estimator will be equal to the actual phase of the signal. The LSE estimator is efficient or precise in that, the estimator variance reaches the Cramér-Rao lower bound for estimator performance for large number of iterations.

5.1.2.4 Phase stability results

Initially, the downconverter was placed in the lab's ambient temperature control while phase and temperature data were acquired overnight. Figure 5.13 shows a plot of the inter-channel phase difference and the ambient temperature acquired in this way. Best quadratic fits to both sets of data are also plotted. The lab ambient temperature control is an on-off feedback control, which from control theory, gives

a sinusoidal response in temperature. This is evident from Figure 5.13. A more interesting fact however, is that the inter-channel phase is not only highly correlated to changes in ambient temperature, but also very sensitive to it. The inter-channel phase standard deviation in this experiment was about 330 mdeg, significantly higher than the design specification. This means that to meet the specification, either a constant ambient temperature has to be assured or some sort of active temperature calibration is required.

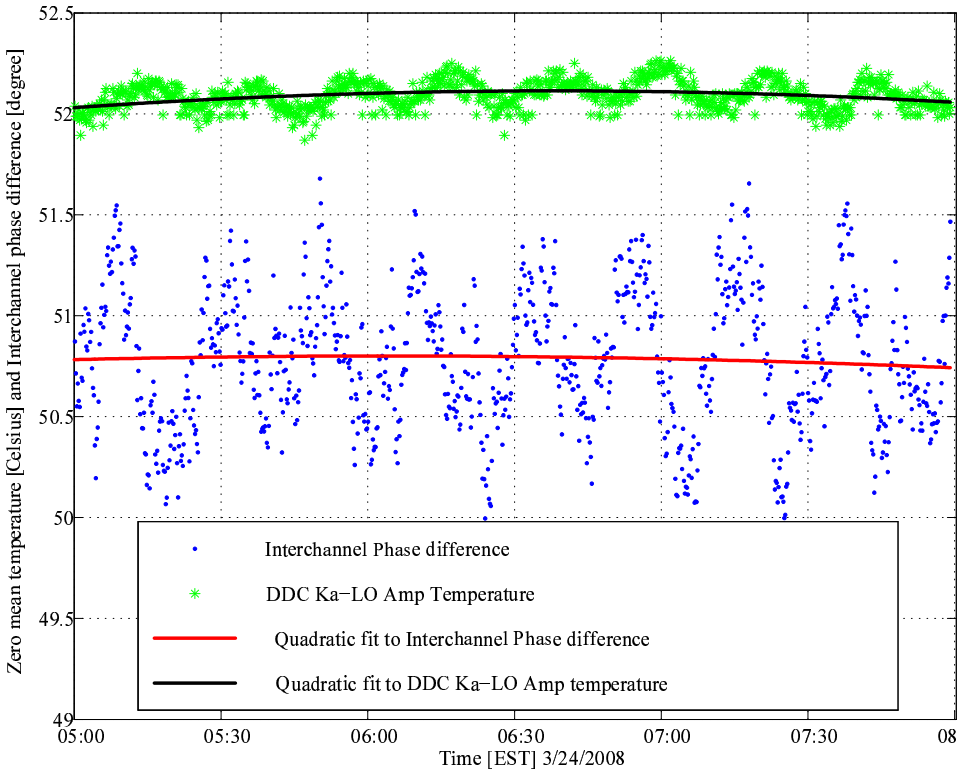

Figure 5.13. Plot of the Ka-band dual downconverter's inter-channel phase and the ambient temperature in the lab

To isolate the dual downconverter from the ambient temperature variations, it was put into an insulated cooler box. The cables to and from the downconverter were passed from a hole sealed with foam. This setup did not have the sinusoidal temperature variations. The downconverter however, dissipated heat which was trapped

inside the cooler box increasing its temperature steadily. A few bags of ice and a fan for air circulation were employed to reach lower temperatures. Results from one such experiment are shown in Figure 5.14. The inter-channel phase standard deviation from the best quadratic fit was about 30 mdeg, which is within the required specification. This suggests that if there is a way to thermally calibrate out the trend in inter-channel phase due to temperature changes, the required phase stability can be attained. This is of course assuming that such a calibration is valid, which might not be the case, especially in the presence of temperature transients.

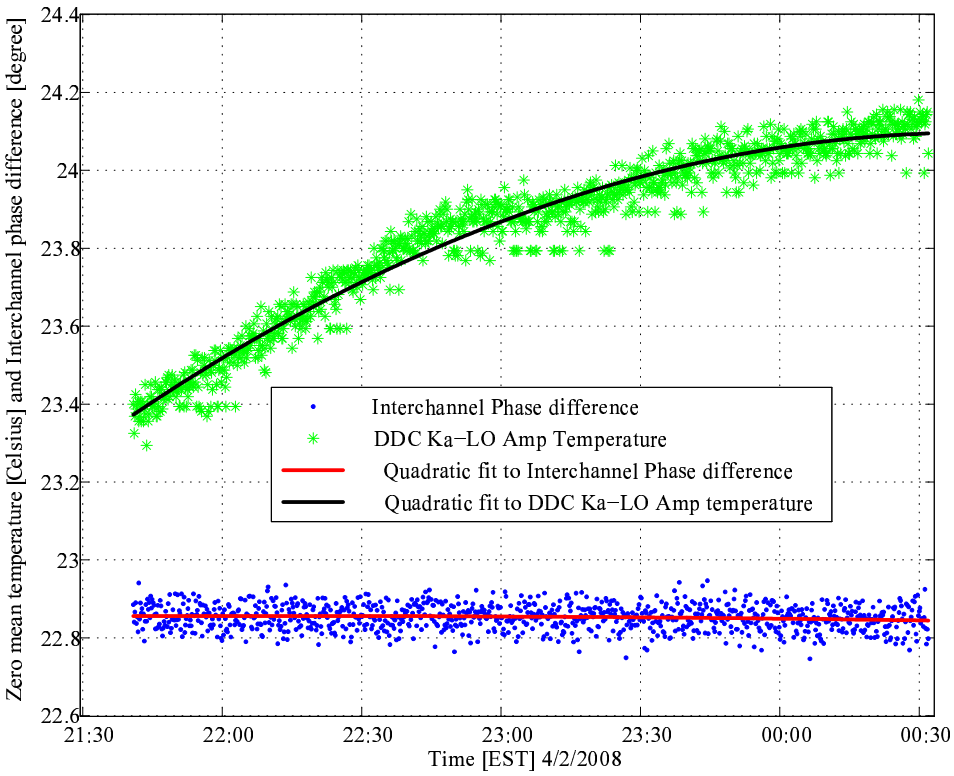

Figure 5.14. Plot of the Ka-band dual downconverter's inter-channel phase and the ambient temperature inside the insulated cooler box

The cooler experiment proved that if the temperature related trend were taken out of the inter-channel phase, then the required phase stability can be achieved. In order to make a repository of inter-channel phase values at various temperatures

over the entire bandwidth for possible temperature-frequency-phase calibration, experiments with controlled temperature profiles are required. To accomplish this, the EC12 temperature chamber was procured. The EC12 was programmed to sweep the chamber temperature according to predetermined profiles. Figure 5.15 shows two such runs on different days. With a correlation coefficient between profiles of almost unity, the EC12 can create repeatable temperature profiles. However, the

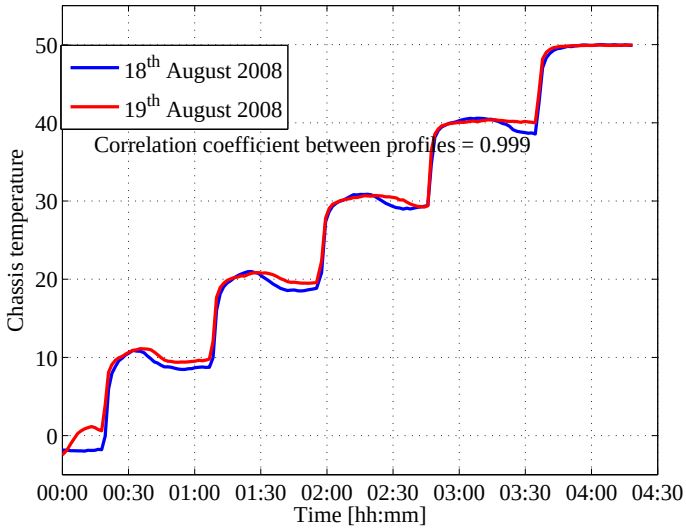

Figure 5.15. Repeatability in temperature profiles inside the EC12

active temperature control inside the EC12 does create some problems. The PID (proportional-integro-differential) controller in the EC12 turns on and off a heating or cooling element. This creates small but significant ripples in the chamber temperature even when it is intended to keep the temperature constant. The amount of ripple in chamber temperature when the EC12 is commanded to hold the temperature constant depends on the power dissipation inside the chamber (by the downconverter) and on the difference between the chamber temperature and the room temperature. One such example of ripples, or rather spikes is shown in Figure 5.16. The figure also shows the inter-channel phase difference. The phase difference remains constant when the temperature is held constant at 30°C. When the temperature transitions

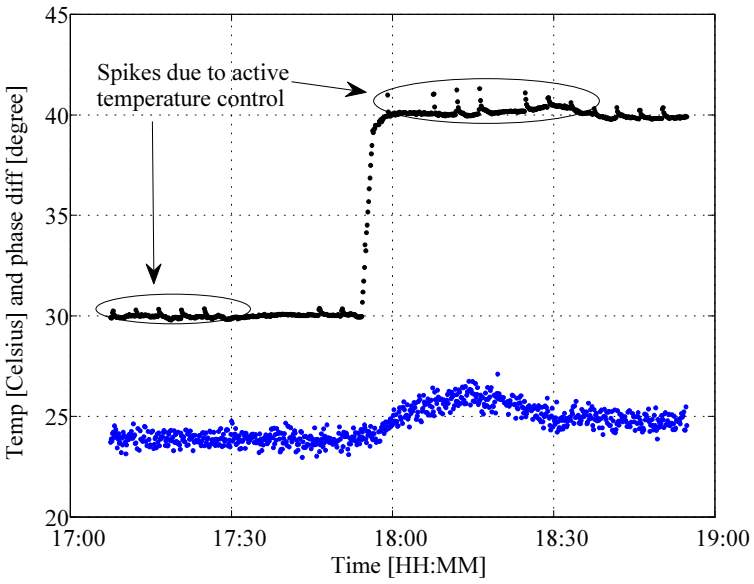

Figure 5.16. Temperature spikes due to the active thermal control in the EC12

from 30°C to 40°C, the thermal inertia of the system results in differential heating transients between the two channels, and the phase difference changes drastically. Once the temperature settles at 40°, the differential temperature reaches a steady value, and the phase difference settles at another value. The phase standard deviation when temperature is held constant was found to be about 300 mdeg- almost the same as the case with the ambient temperature control of the lab air-conditioning. This perhaps, is because the temperature ripple in Figure 5.16 is of the same order of magnitude as the ripple in Figure 5.13. Although the phase standard deviation inside the EC12 does not meet the specification, the average value of phase can be used for possible temperature-frequency-phase calibration. Results of an experiment attempting such a calibration follow.

Four experiments were carried out on four different days- 18^{th}, 19^{th}, 20^{th}, and 21^{st} of August 2008. The temperature profiles used on the 18^{th} and 19^{th} are shown in Figure 5.15. The temperature profiles used on the 20^{th} and 21^{st} are similar to those in 5.15, the only difference being that the temperature was held constant on the steps for an hour instead of 45 minutes. A host of parameters such as RMS amplitude, phase,

frequency error, rms error from least-squares fit for both channels were computed and stored continuously throughout the profile. These measurements and estimations were made at 10 baseband frequencies from 105 MHz to 5 MHz. Figure 5.17 shows a scatter plot of the inter-channel phase at three different frequencies versus temperature from data acquired from the experiments on the 20^{th} and 21^{st}. This plot shows that the

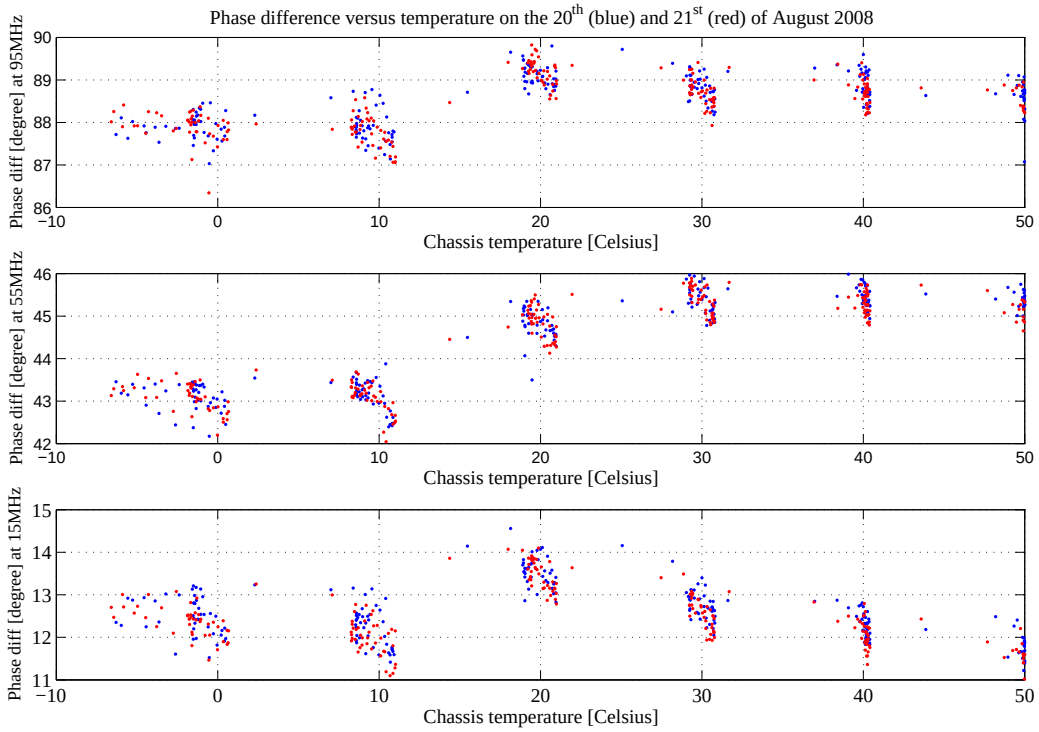

Figure 5.17. Plot of the inter-channel phase versus temperature using data from the 20^{th} and 21^{st} of Aug 2008

phase data from the 20^{th} is consistent with that from the 21^{st}. This suggests that a temperature-phase type calibration at different frequencies is possible if a data base from such experiments is assimilated. Figure 5.18 shows a similar scatter plot that uses data from the experiments carried out on the 18^{th}, 19^{th}, and 20^{th}. Consistency is seen in this plot too despite the fact that the temperature profiles on the 19^{th} and 20^{th} were slightly different.

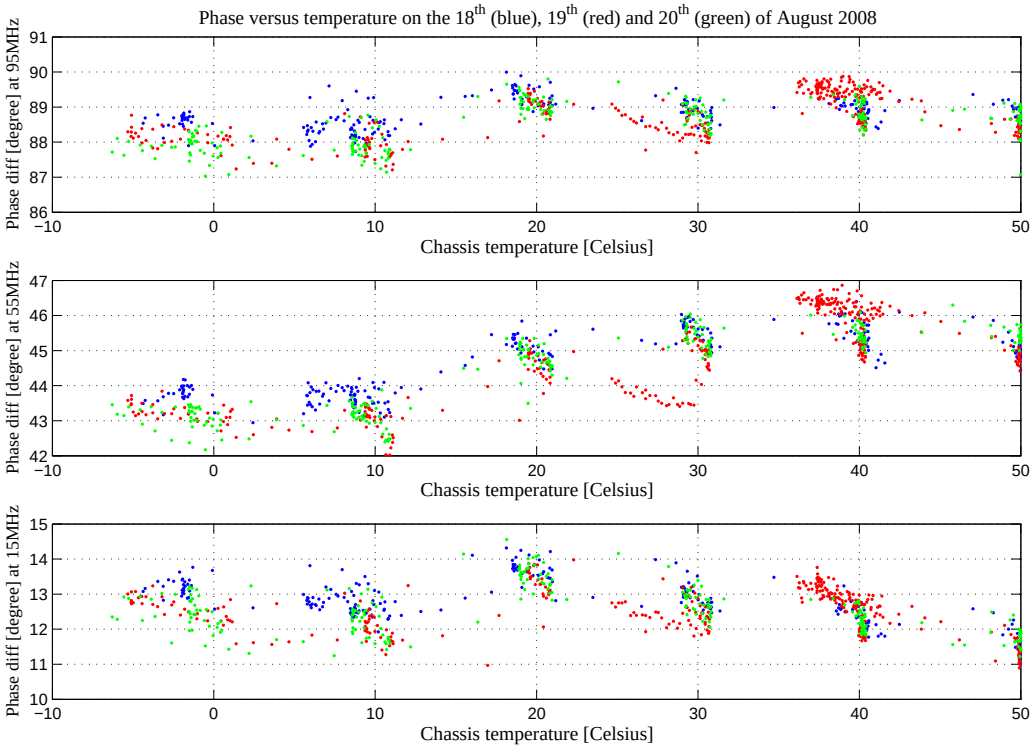

Figure 5.18. Plot of the inter-channel phase versus temperature using data from the 18^{th}, 19^{th}, and 20^{th} of Aug 2008

Figures 5.17 and 5.18 involve all points on the temperature profile that include points along the transition from one temperature to another. To better understand the static temperature-phase response of the downconverter, points on the horizontal line in Figure 5.15 having a steady and constant temperature ($\pm 0.5°$C) were grouped together. The mean and standard deviation of each group was computed at the three frequencies for the data from 18^{th} and 19^{th}. This was repeated for the data from 20^{th} and 21^{st}. These results are shown in Figure 5.19 and Figure 5.20.

The mean value of inter-channel phase is consistent between experiments at all three frequencies. The standard deviation of the inter-channel phase is however high, perhaps due to the active temperature control as mentioned earlier. To understand how good a calibration is possible with the available data, the difference between

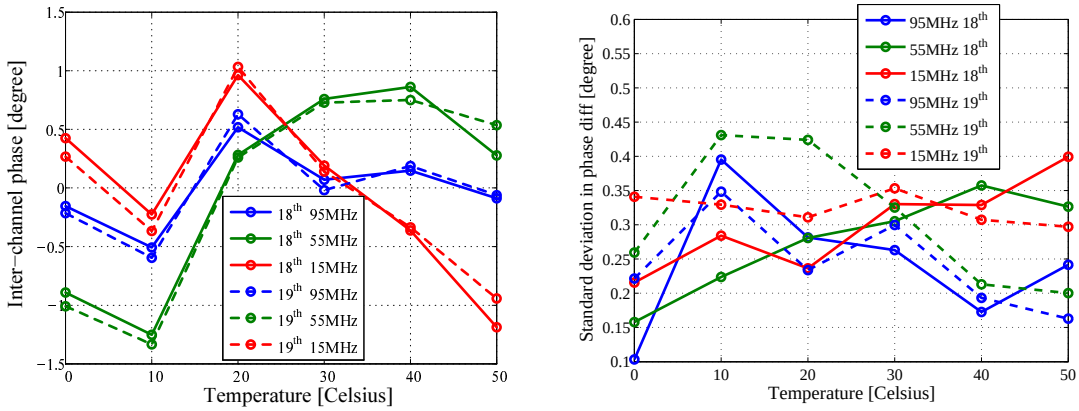

Figure 5.19. Plot of the average (left) and standard deviation (right) of the inter-channel phase versus temperature for data from the 18^{th} and 19^{th} of Aug 2008

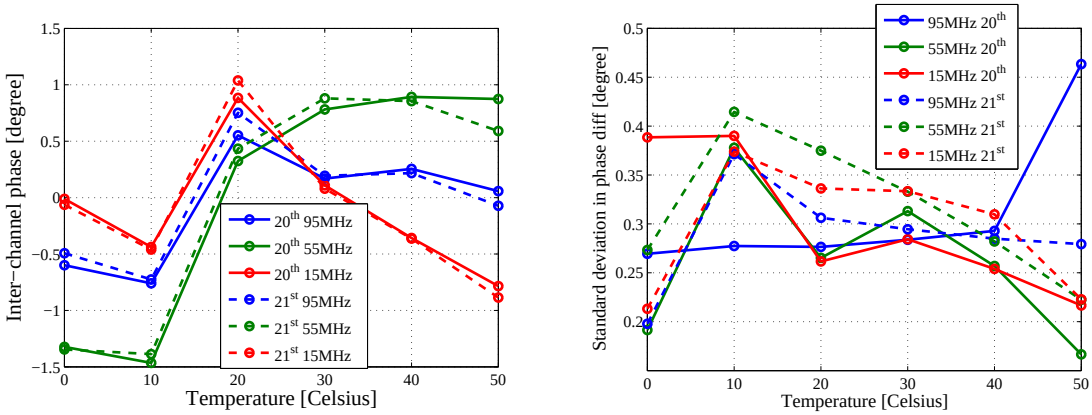

Figure 5.20. Plot of the average (left) and standard deviation (right) of the inter-channel phase versus temperature for data from the 20^{th} and 21^{st} of Aug 2008

the mean phase-difference values in Figures 5.19 and 5.20 are plotted in Figure 5.21 This shows that the calibration error between days can be as high as 500 mdeg, requiring a more short-term calibration. An experiment in a more controlled thermal environment therefore would be an important next step. This may be accomplished by a thermal blanket to increase the thermal inertia of the system thereby minimizing the temperature spikes.

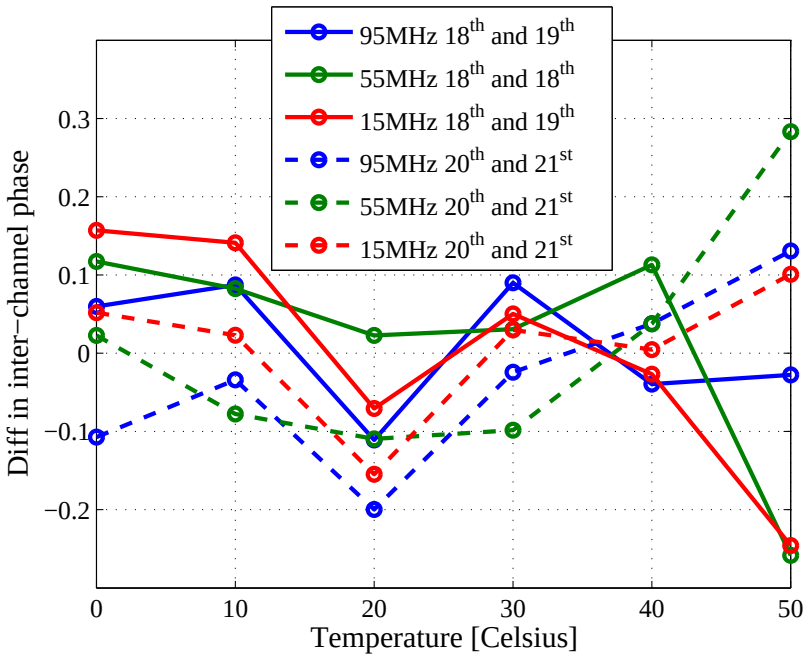

Figure 5.21. Difference between the average inter-channel phase of 18^{th} and 19^{th}, and between that of 20^{th} and 21^{st}.

5.2 Antennas

The antennas were evluated in the lab for return loss and radiation pattern. The antenna is a one-port device with the far end of the waveguide ending in a sliding short. The short must be positioned at the right distance ($\frac{\lambda_g}{4}$, $\frac{3\lambda_g}{4}$, $\frac{5\lambda_g}{4}$. . . .) from the last slot in order for the antenna to be matched and for the standing wave in the antenna to illuminate all slots equally producing a symmetric broadside beam. The sliding short used had enough travel distance to match the antenna by placing the short at $\frac{\lambda_g}{4}$, $3\frac{\lambda_g}{4}$, and $\frac{5\lambda_g}{4}$ from the last slot. A plot of the input reflection coefficient for these three cases is given in Figure 5.22.

The radiation pattern of the antennas was measured in a near field range at the Antennas and Propagation Laboratory, UMass, Amherst. The near field range measured the near field pattern of the antenna and uses the Fourier transform relationship between the antenna near field pattern and far field pattern to compute the far field

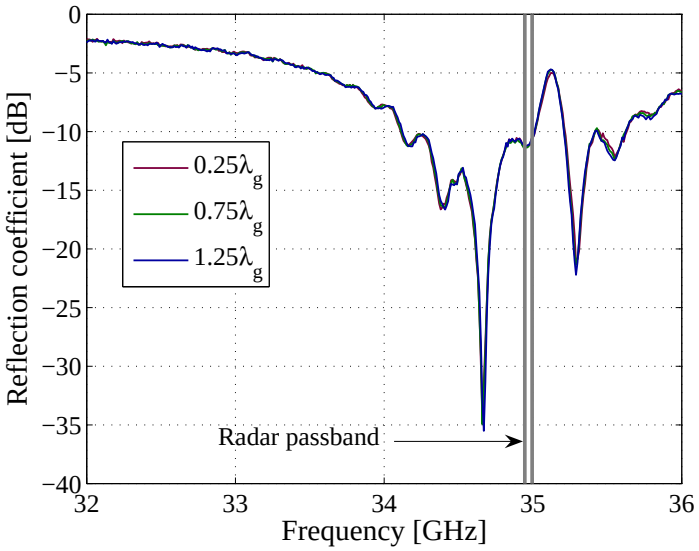

Figure 5.22. Measured reflection coefficient of the interferometer antenna

radiation pattern. The NSI 2000† software does these computations and also provides a user console for controlling the measurement setup. The normalized E-plane and H-plane patterns thus measured were compared with the theoretical patterns as shown in Figure 5.24.

The theoretical E-plane pattern in Figure 5.24 was obtained from the theory presented in Chapter 4. The theoretical H-plane pattern was obtained from the element pattern and the array factor. The element pattern of a slot was assumed to have the same radiation pattern as that of a half-wavelength dipole, which is an accurate assumption if the slot were infinitesimally thin with an infinite ground plane. This approximation does not induce considerable error as the antenna pattern is primarity dictated by the array factor. The radiation patterns in Figure 5.24 show good agreement between the theoretical and measured patterns. The beamwidth in the E-plane and H-plane are 45° and 0.95° which meet design specifications. It is imperative to point out that the assymetry in the H-plane pattern and its sidelobe

†By Nearfield Systems Inc., Torrance CA

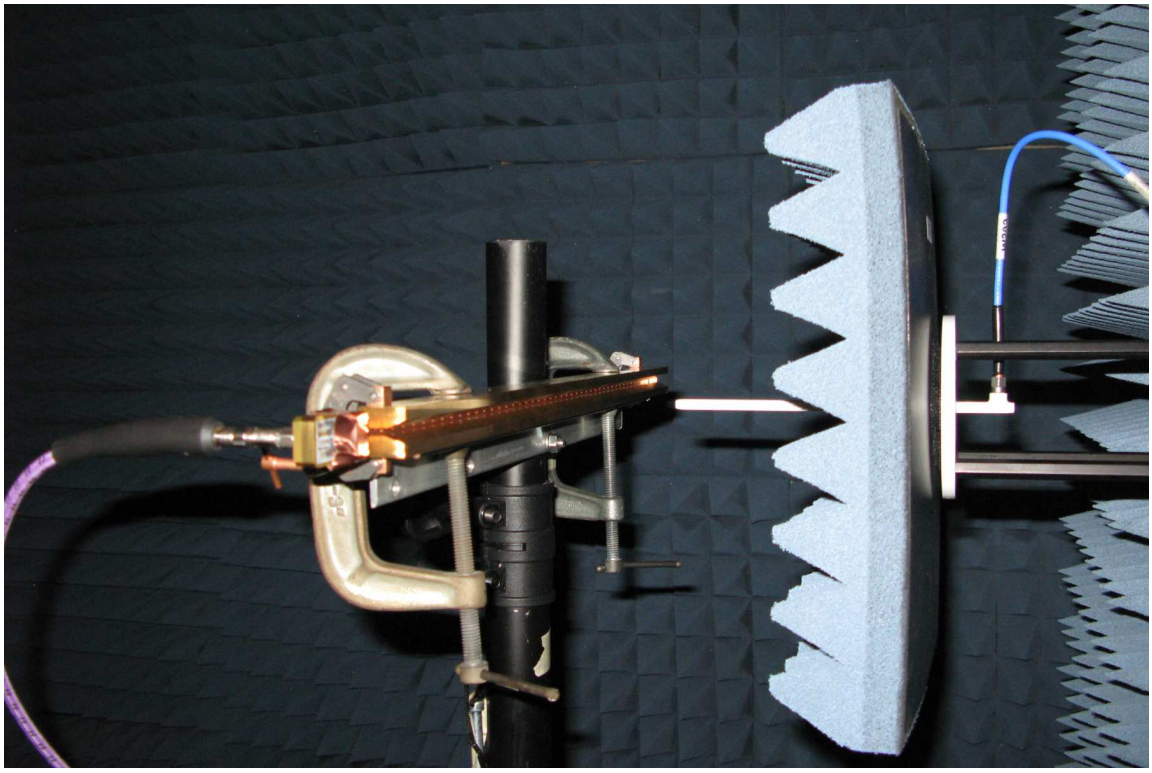

Figure 5.23. Picture of the antenna in the near field range anechoic chamber

levels are due to unsymmetric illumination of the slots by the standing wave in the antenna. This is primarily an artifact of mismatch arising due to the short on the far end of the antenna not being precisely at a quarter guide wavelength distance from the last slot. This was indeed the case during the antenna pattern measurement due to non-availability of a sliding short forcing the use of a fixed short at an approximate distance from the last slot[†].

[†]The sliding short was later procured and used in the matching measurements of Figure 5.22. A final antenna pattern measurement with this sliding short in place is imperative, and Figure 5.24 should be regarded as an approximate result.

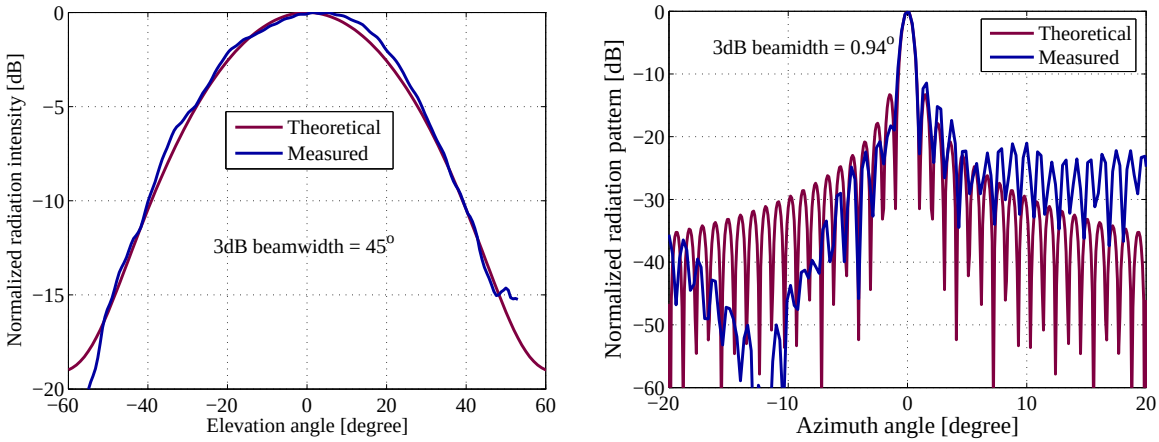

Figure 5.24. Measured and theoretical E-plane (left) and H-plane (right) radiation patterns for the interferometer antenna

CHAPTER 6

FIELD DEPLOYMENT

The final near term (year of 2009) goal of the UMass Ka-band interferometer is an airborne deployment. Before such an expedition, it is desirable to evaluate the instrument in a simpler deployment on ground or on a rooftop. Such a deployment would not only serve as a proof of concept, but also provide insight into the dominant error sources and some of the more practical issues important to field deployment of such an instrument. With this in mind, the UMass Ka-band interferometer was deployed on the ground looking up at a building and also atop a building looking down on the landscape around it. This chapter discusses the mechanical mount and positioning equipment used for these deployments and presents first results from these experiments.

6.1 Mechanical mount

The fundamental principle of interferometry uses geometric transformations to estimate target height. Knowledge and control over the interferometer geometry is a pivotal factor to a successful measurement as discussed in Chapter 2. The makes the mechanical mount for the radar a critical aspect of any field deployment. This mechanical mount must provide a variable yet stable baseline length, baseline angle, and look angle. Figure 6.1 shows a picture of the mechanical mount for the UMass Ka-band interferometer.

The entire mount is made of Aluminum to minimize weight. The three interferometer antennas are supported using two parallel vertical bars. The antennas are

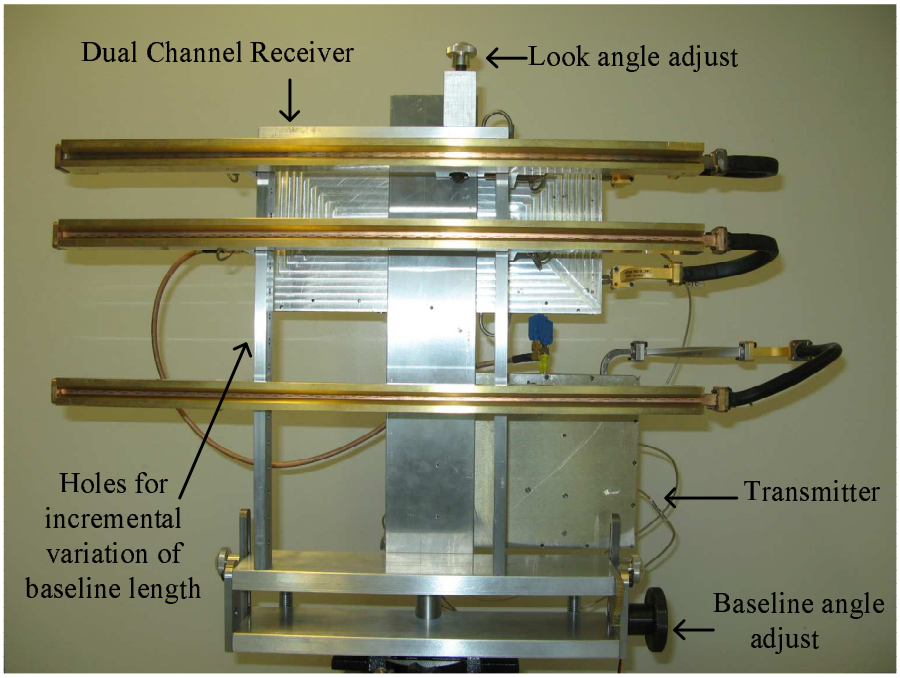

Figure 6.1. Picture of the mechanical mount for the interferometer's rooftop deployment

fastened at both bars using a hole and push-button pin arrangement such that, they can be fastened and unfastened with ease. Both the vertical bars have an identical set of pin-holes separated by 20mm along a length of about 300mm. By fastening the antennas on different hole pairs, the baseline length can be varied in increments of 20mm. The baseline angle is varied by rotating (in elevation) the entire platform on which the antenna, vertical bar arrangement, transmitter and DDC sit. This is facilitated by a hand operated knob that transfers its rotation to the platform through a gear link. Apart from these two degrees of freedom, the look angle of the antennas is variable and changed in unison such that the three antenna-beams point to the same direction in elevation. This rotation is facilitated by a mechanical link between the three antennas that runs parallel to the two vertical bars. The vertical motion of the link is converted into elevational rotation in the antennas; the rotation pivot being the link fastening the antennas to the vertical bars. This link is made such that when

the look angles of the antennas are varied (by rotating a knob), they always point their beams at the same elevation angle.

The positioner used for the radar is a telescope positioner mounted on a tripod. One of the axes on the positioner is used for azimuth scanning. The radar with its mechanical mount is mounted on this positioner with a custom mating bracket. This telescope positioner was not found to be sturdy enough, as its elevation angle changed over time due to torque from the radar's weight. Moreover, the features available for command and control of the positioner are more suited for telescope positioning. To address these issues, a new positioner more suited for radar positioning has been procured,[†] and will be integrated with the radar for the next field experiment.

6.2 First results

The radar transmitter, downconverter, and the NI-PXIe system[‡] were integrated and deployed on ground outside the lab[§]. The aim of this deployment was to verify whether the various subsystems worked together to make a radar. The radar scanned an azimuth sector containing a parking lot and a tall building. Later, the radar was deployed on a building (LGRT) with an aim to obtain interferometric phase fringes verifying that the instrument works as an interferometer. First results from these deployments are documented below.

6.2.1 Ground deployment

Figure 6.2 shows a picture of the UMass Ka-band interferometer deployed outside the laboratory looking at a parking lot, trees, and the LGRT building. An aerial

[†]The Sentry 90 from QuickSet International Inc.; datasheet can be found in [5].

[‡]The author expresses his acknowledgements to Mike Shusta, an undergraduate student of electrical engineering at UMass, Amherst for his diligent LabView programming of the NI-PXIe system.

[§]Knowles engineering building, UMass Amherst (see Figure 6.2)

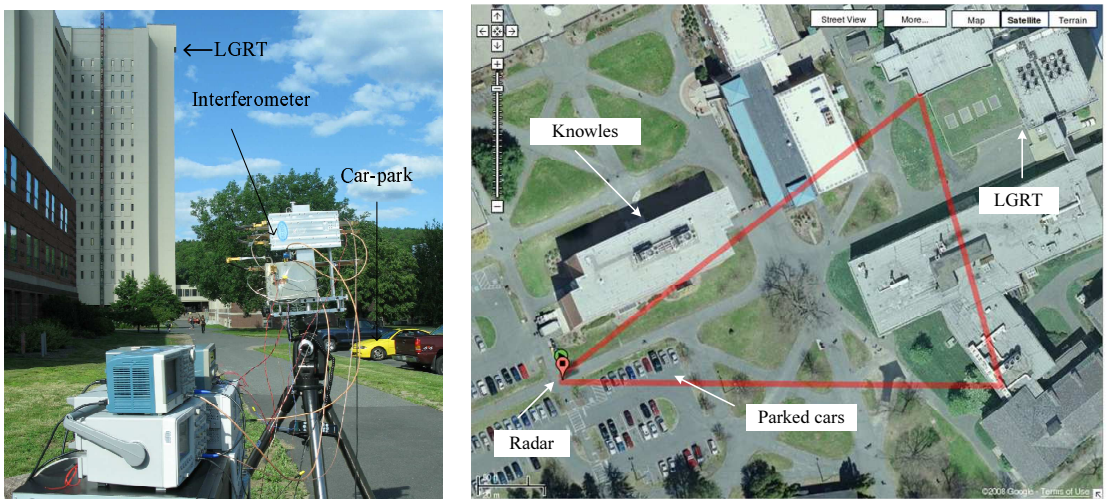

Figure 6.2. Picture of the UMass Ka-band interferometer deployed on ground (left) and an aerial picture (from http://maps.google.com) of the deployment site (right)

view of the deployment site from google maps is also shown. Some of the prominent features that are apparent on the radar image are labeled in these pictures. Since this was the first deployment, pulse compression was not implemented for two reasons. Firstly, a basic pulsed radar is easier to implement. Secondly, and more importantly, the intended targets would have gone undetected within the blind range of the radar even in case of the fastest frequency chirp within the capability of the radar handware. A pulsed radar with a pulse width of 16 ns was implemented. This corresponds to a baseband waveform having one cycle of a sine-wave at 60 MHz. Baseband here refers to the frequency band at the output of the dual downconverter or equivalently, the input of the transmitter. The signal obtained after IQ detection of this baseband signal is referred to as the complex-baseband to avoid confusion. The IQ-demodulation process is depicted in Figure 6.3. The baseband time series consists of a gated sinusoid that is represented by a sinc function in the frequency domain centered at $f_c = 60$ MHz. This baseband time series is first multiplied by an exponential to shift its center frequency to 0 Hz. The resulting waveform is then low-pass filtered to retain only the main lobe of the sinc function that contains most

of the signal's information. This filtering also eliminates out of band interference and spurious mixing products. The signal thus obtained is the complex-baseband signal that is used to form the interferogram.

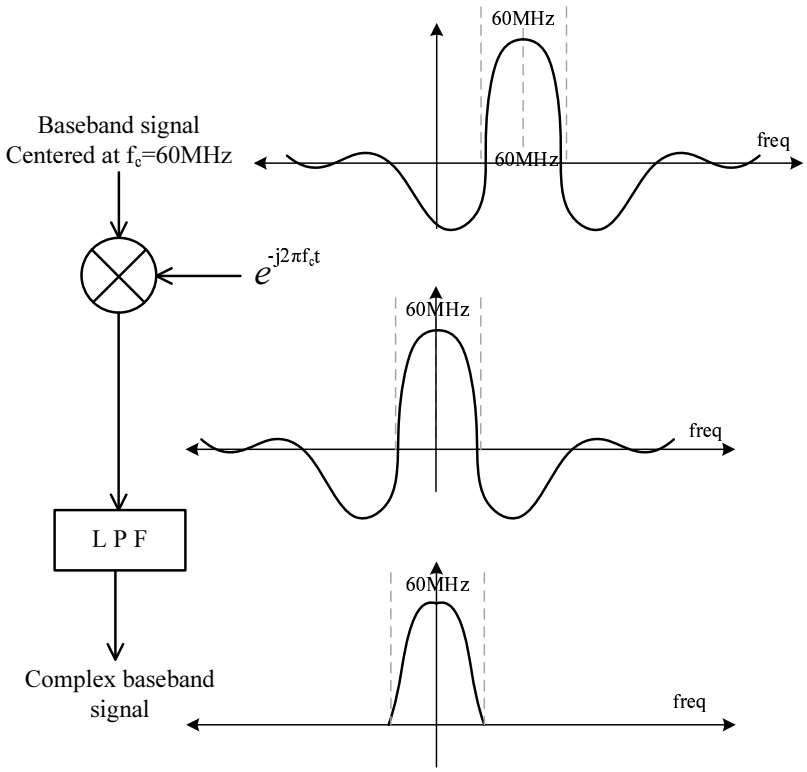

Figure 6.3. Depiction of the IQ-demodulation process employed for the ground deployment experiment

Several data acquisitions were made with a receive window of 2 μs (maximum range of 300m) and a sampling rate of 1 GS/sec. The positioner swept out an azimuth arch with the radar collecting data pulses every 0.25°. There were 512 pulses acquired at every azimuth position. This results in a complex two dimensional array of complex-baseband signal for every azimuth position. One dimension being the "short-time" index or radar sampling time index, and the other dimension being the "long-time" index or the radar pulsing time index. This 2D array from one channel is multiplied element by element to the conjugated 2D array from the other channel to form the element by element correlation. The argument of the elements in the

resulting 2D matrix has the interferometric phase information. The correlation coefficient over the long-range dimension was then computed for this 2D array. Targets which do not move a considerable fraction of a wavelength over times scales of the PRF (1 kHz) give rise to a consistent interferometric phase every pulse, and hence a strong correlation coefficient. On the other hand, those range bins having moving targets such as grass and leaves, or those dominated by thermal noise, do not correlate well temporally on pulse-to-pulse time scales. A plot of the magnitude and angle (interferometric phase) of the temporal correlation coefficient for the ground deployment experiment is shows in Figure 6.4. Some of the prominent targets are

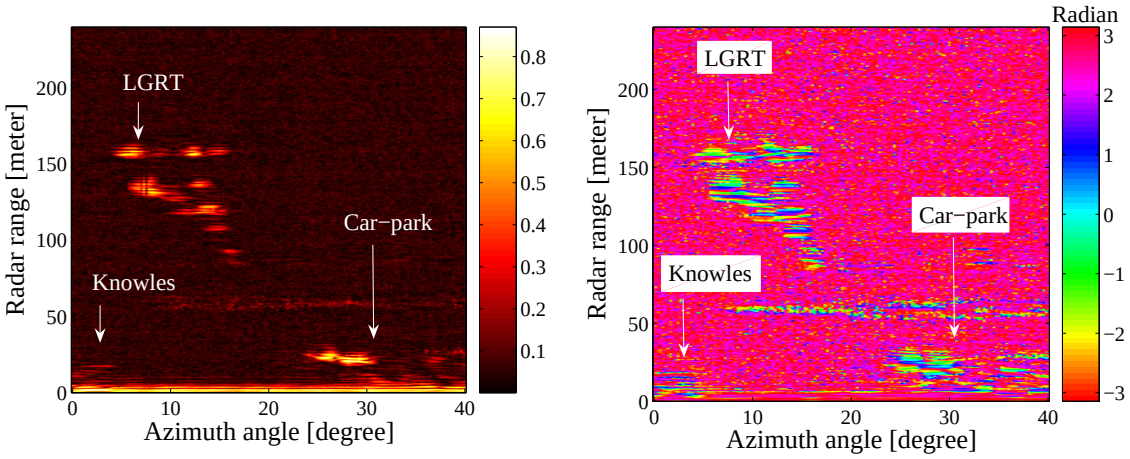

Figure 6.4. Magnitude (left) and angle (right) of the temporal correlation coefficient between the two interferometric channels for the ground based deployment

identified in Figure 6.4. These identifications were made on the basis of visual knowledge of the targets' bearing, and by comparing the radar range to range measured by a stereoscope. It can be seen in Figure 6.4 that stationary targets like buildings and cars are highly correlated temporally, whereas grass and trees are not temporally correlated. The most promising aspect of the correlation plots are the smooth phase-fringes on stable targets such as the LGRT. While the high correlation magnitude on such targets suggests that the interferometric phase information in them is reliable,

the interferometric phase itself shows that the instrument works successfully as an interferometer in a basic sense.

In the ground deployment discussed above and the rooftop deployment that is discussed below, there was no switch employed at the output of the transmitter. The transmitter antenna to receiver antenna isolation was sufficient to protect the LNA from being damaged. However, the transmitter was sending out spurious ringing oscillations even after the transmit pulse ended. This coupled into the receiver and competed with the weak echo within the finite dynamic range (8bits) of the data acquisition module, as a result of which, only strong targets such as buildings could be detected, and reliable interferometric fringes spanning the whole range-azimuth space could not be obtained. This problem with the transmitter is currently being investigated.

6.2.2 Rooftop deployment

The ground based deployment showed that the radar works as an interferometer in a basic sense. Despite the shortcoming in the transmitter, a rooftop deployment was made on the top of the Lederle Graduate Research Center (LGRT). Figure 6.5 shows a view from the top of the LGRT looking down North-West. The rooftops of some of the smaller buildings make strong and coherent targets. A pulsing, data acquisition and processing scheme similar to the one used in the ground deployment was employed. The magnitude and phase of the temporal correlation thus obtained is shown in Figure 6.6. Consistent interferometric-fringes on building rooftops has been an encouraging result. The problem with the transmitter however persisted allowing only strong targets such as building edges to be apparent on the interferometric images. A detailed height map of the landscape around the LGRT could be obtained if this problem is solved. This is the current focus of the ongoing research work.

Figure 6.5. Picture of the UMass Ka-band interferometer deployed on the rooftop of the LGRT

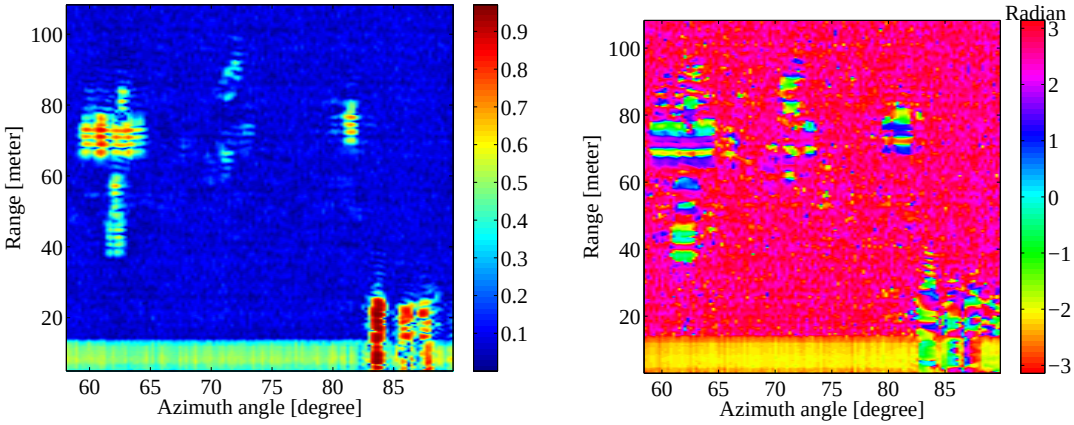

Figure 6.6. Magnitude (left) and angle (right) of the temporal correlation coefficient between the two interferometric channels for the rooftop deployment

CHAPTER 7

CONCLUSIONS AND FUTURE WORK

The work documented in the above pages is a part of an ongoing research effort to use dual frequency interferometric measurements at Ku- and Ka-band to estimate topography and snow physical parameters in the earth's cryosphere. Documented herewith in this thesis is a module of this research effort that involves the design, development, and evaluation of the Ka-band interferometer instrument. Conclusions drawn from this work and recommendations for future work will serve as a reference and guideline for future research efforts.

7.1 Summary of work

Ka-band interferometry is a suitable radar technology for many remote sensing measurements currently required by the scientific community. Due to technological challenges involved in interferometry at millimeter-wave frequencies in terms of hardware design and evaluation, there has not been a successful demonstration of interferometry at Ka-band in the open literature. An ongoing effort at the Microwave Remote Sensing Lab at the Univ of Massachusetts, Amherst to refine the design, evaluation, and deployment of a Ka-band interferometer for cryospheric applications aims at providing a proof of concept and benchmark for future airborne and spaceborne missions. Work accomplished towards this effort is summarized below.

(i) The theory of topographic mapping using cross-track interferometry was studied. The constraints and considerations in choosing key parameters related to instrument hardware and deployment geometry were understood and analyzed.

Using the relationship between these parameters and the instrument error, resolution, and sensitivity, a configuration for the instrument in terms of deployment geometry and hardware architecture was arrived at.

(ii) The remainder of the work involved building, integrating, and testing the hardware subsystems, and initial field deployments of the instrument. Four-layered Printed Circuit Boards (PCB) for the downconverter (receiver) and upconverter (transmitter) were designed and fabricated. A custom mechanical housing for the two downconverter PCBs (one for each stage of downconversion) was designed and manufactured. A temporary housing for the transmitter was built in-house at MIRSL.

(iii) A suitable backplane, controller, chassis, and signal generation and data acquisition modules were identified for a NI-PXIe system making up the baseband digital electronics. The system was programmed for radar signal generation, RF data acquisition, telemetry data acquisition, and radar timing and control. This system was later integrated with the other hardware blocks of the radar.

(iv) After the design and fabrication of the various hardware blocks, each one of them was tested in the laboratory and their performance was compared with the initial design specifications. The downconverter being the most performance critical part of the radar was the subject of bulk of the lab testing and evaluation. The downconverter's bandpass characteristics such as input RF return loss, noise figure, image rejection ratio, output non-linearity, and gain variation were measured across the radar bandwidth.

    (a) The input return loss met the design specifications in spite of undesirable twist in the input connector due to external torques resulting from wear and tear.

(b) An accurate measurement of noise figure was not possible due to non-availability of a calibrated hot and cold noise source at Ka-band. However, the direct measurement method was employed, and owing to high measurement uncertainties, it was not conclusive whether the instrument noise figure met design specification over the entire radar bandwidth. The measured noise figure however was not worse than within 1dB of the specified maximum in spite of the measurement uncertainties.

(c) The downconverter was found to be well within the linear region for the specified range of input power. The relative power in the second and third harmonics was measured over the radar bandwidth.

(d) Image rejection ratio for four possible image bands (resulting from two stages of downconversion) were measured. The image rejection ratio for three of the four image bands were within specifications. The fourth image band could not be rejected by image reject filters at the L-band due to the high radar bandwidth coupled with proximity of the L-band RF band to the L-band LO. Further, an image reject mixer could not be employed due to non-availability of hybrids at the baseband frequency and bandwidth. The design specifications however, could be met at the reduced radar bandwidth of 20 MHz according to the ACT specifications by using a suitable L-band image reject filter used.

(e) Gain flatness over a radar bandwidth of 100 MHz did not meet the rather ambitious specification of 2dB. This specification was easily met for the ACT specified bandwidth of 20 MHz.

(v) The next set of downconverter evaluation measurements were the thermal tests. The downconverter output amplitude and phase were monitored as the ambient temperature changed. The channel gain for both channels and the differen-

tial gain at various temperatures in the specified thermal operating range were measured and a look up table for future calibration was created. The channel phase and inter-channel phase at different temperatures was a more involved measurement. The experimental setup and algorithms for phase measurement from a previous work [12] were studied and adapted for the required measurements. The inter-channel phase from the ensuing measurement was found to be very sensitive to the lab ambient temperature cycles. The inter-channel phase standard deviation was found to be about 300 mdeg. This did not meet the design specification of 50 mdeg. The downconverter was then thermally isolated in a cooler box, and the inter-channel phase standard deviation from the best quadratic fit was measured to be 30 mdeg which meets design specifications. This proved that the hardware, experimental setup and estimation algorithms used could meet the design specification if the trend in inter-channel phase due to temperature could be calibrated out. Controlled thermal profiles required for such a calibration were setup using the EC12 environmental chamber. The repeatability in the attempted calibration could not be kept within 50 mdeg primarily because of the temperature transients arising out of the active temperature control inside the chamber. The results from these experiments were nevertheless documented for future reference.

(vi) A brief literature survey was carried out to understand the analytical formulation and underlying physics behind the slotted waveguide antenna design. The antenna was designed using both analytical techniques and HFSS simulations. The antenna pattern and return loss were measured and were found to agree well with the design specifications and theoretical values.

(vii) A mechanical mount for the antennas, transmitter, and receiver was designed and manufactured. The mount could provide baseline length and angle varia-

tion, and antenna look angle variation. The radar and its mount were deployed on ground and on the rooftop of the Lederle Graduate Research Center (LGRT) at UMass using a tripod telescope positioner. The data thus acquired was processed to generate interferograms. The results from these experiments revealed some of the the flaws in the transmitter and the positioner. However, the data showed smooth phase fringes on stable targets conforming that the various radar subsystems work together as an interferometer.

7.2 Recommendations for future work

The ground based and rooftop deployments were only the first and most basic of the many upcoming deployments for the UMass Ka-band interferometer. Moreover, there is some rework and upgrade required in the current hardware and software. These comprise the intended future work and are elaborated below.

(i) The current transmitter gives out spurious oscillations after the transmit pulse. This problem will be investigated. The first stage of upconversion in the transmitter has a double side-banded output. One of the side-bands cannot be filtered efficiently due to the high signal bandwidth and close proximity of the signal to the LO. A better upconverter could employ a direct single sideband upconverter that accepts in-phase and quadrature-phase baseband inputs from the direct digital synthesis of the baseband frequency chirp. A new transmitter board with this upgrade has already been designed and fabricated. This board is current undergoing laboratory evaluation.

(ii) The new transmitter PCB has been made such that the current downconverter chassis can be adapted to suite the transmitter with minimal changes. This would in future enable the transmitter to have its own precision machined custom housing. Parts and equipment needed to house the transmitter, receiver, LO

generation, and power supply in a weather proof enclosure have been procured. Integrating this enclosure with the radar and positioner will enable deployments in inclement weather conditions.

(iii) The telescope positioner suffered from mechanical stability issues and has been discarded. LabView routines to command and control the new Sentry 90 positioner will be written, and the mounting brackets to integrate the positioner with the radar will be machined.

(iv) The rooftop experiment will be repeated with the new transmitter to obtain an elevation map of the landscape that will be compared with ground truth. After the success of such a deployment, the interferometer will be deployed on a mountain cliff. Such a deployment can sustain larger blind ranges and pulse compression will be implemented. A success of such an experiment will put the ongoing research close to an airborne deployment.

BIBLIOGRAPHY

[1] David M. Pozar. *Microwave Engineering*, Third ed. John Wiley & Sons, 2005.

[2] Goldstein, R.M., Zebker, H.A., and Werner, C.L. Satellite radar interferometry: Two dimensional phase unwrapping. *Radio science 23*, 4 (July/August 1988), 713–720.

[3] Graham, L.C. Synthetic interferometric radar for topographic mapping. *Proceedings of the IEEE 62*, 6 (June 1974), 763–768.

[4] Gruenberg, H. Second-order beams of slotted waveguide arrays. *Canadian Journal of Physics 31* (January 1953), 55–69.

[5] Harish Vedantham. TIMMi- Ka-band Dual Down Converter technical document. *Microwave Remote Sensing Lab, UMass, Amherst* (2008).

[6] John F. Ramsay, and Boris V. Popovich. Series-slotted waveguide array antennas. *IRE International Convention Record 11* (March 1963), 30–55.

[7] Karthik Srinivasan Venkatasubramanian. Design and Development of TIMMI- An Interferometric Radar. *Master's Thesis, University of Massachusetts, Amherst* (2007).

[8] Nikolaus P. Faller, and Erich H. Meier. First Results with the Airborne Single-Pass DO-SAR Interferometer. *IEEE Transactions on Geoscience and Remote Sensing 33* (September 1995), 1230–1237.

[9] Oliner, A. A. The impedance properties of narrow radiating slots in the broad face of rectangular waveguide- part i and ii. *IRETransactions on Antennas and Propagation 5*, 1 (January 1957).

[10] Paul A. Rosen, Scott Hensley, Ian R. Joughin, Fuk K. Li, Soren N. Madsen, Ernesto Rodriguez, and richard M. Goldstein. Synthetic aperture radar interferometry. *Proceedings of the IEEE 88*, 3 (March 2000), 333 382.

[11] Paul Siqueira, Razi Ahmed, John W. Wirth, and Alex Bachmann. Variable precision two-channel phase, amplitude, and timing measurements for radar interferometry and polarimetry. *IEEE Transactions on Microwave Theory and Techniques 55*, 10 (October 2007), 2248–2256.

[12] Razi Ahmed. Radar System Characterization: Mathematical Models, Simulations and Verification. *Master's Thesis, University of Massachusetts, Amherst* (2006).

[13] Roger F. Harrington. *Time Harmonic Electromagnetic Fields*. The IEEE Press Series on Electromagnetic Wave Theory. John Wiley & Sons, USA, 2001.

[14] Rogers, A.E.E, and Ingalls, R. P. Venus: Mapping the surface reflectivity by radar interferometry. *Science 165*, 3895 (August 1969), 797–799.

[15] Stegen, R. J. Longitudinal shunt slot characteristics. *Hughes Technical Memorandum*, 261 (November 1951).

[16] Stevenson, A. F. Theory of Slots in Rectangular Wave-Guides. *Journal of Applied Physics 19*, 1 (January 1948), 24–38.

[17] Watson, W. H. *The physical principles of waveguide transmission and antenna systems*. Clarendon press, London, U.K, 1949.

[18] Zebker, H.A., and Goldstein, R.M. Topographic mapping from interferometric SAR observations. *Journal of Geophysical Research 91*, B5 (1986), 4993–4999.

[19] Zisk, S. H. A new Earth-based radar technique for measurement of lunar topography. *Moon 4*, 3-4 (September 1972), 296–306.